The Astrophysical Journal Supplement Series, 173:415–431, 2007 December

THE STAR FORMATION AND EXTINCTION COEVOLUTION OF UV-SELECTED GALAXIES OVER $0.05 < z < 1.2$

D. Christopher Martin,[1] Todd Small,[1] David Schiminovich,[2] Ted K. Wyder,[1] Pablo G. Pérez-González,[3] Benjamin Johnson,[2] Christian Wolf,[4] Tom A. Barlow,[1] Karl Forster,[1] Peter G. Friedman,[1] Patrick Morrissey,[1] Susan G. Neff,[5] Mark Seibert,[1] Barry Y. Welsh,[6] Luciana Bianchi,[7] José Donas,[8] Timothy M. Heckman,[9] Young-Wook Lee,[10] Barry F. Madore,[11] Bruno Milliard,[8] R. Michael Rich,[12] Alex S. Szalay,[9] Sukyoung K. Yi,[10] Klaus Meisenheimer,[13] and George Rieke[3]

Received 2007 January 21; accepted 2007 July 27

ABSTRACT

We use a new stacking technique to obtain mean mid-IR and far-IR to far-UV flux ratios over the rest-frame near-UV, near-IR color-magnitude diagram. We employ COMBO-17 redshifts and COMBO-17 optical, *GALEX* far- and near-UV, and *Spitzer* IRAC and MIPS mid-IR photometry. This technique permits us to probe the infrared excess (IRX), the ratio of far-IR to far-UV luminosity, and the specific star formation rate (SSFR) and their coevolution over 2 orders of magnitude of stellar mass and over redshift $0.1 < z < 1.2$. We find that the SSFR and the characteristic mass ($\mathcal{M}_0$) above which the SSFR drops increase with redshift (downsizing). At any given epoch, the IRX is an increasing function of mass up to $\mathcal{M}_0$. Above this mass the IRX falls, suggesting gas exhaustion. In a given mass bin below $\mathcal{M}_0$, the IRX increases with time in a fashion consistent with enrichment. We interpret these trends using a simple model with a Schmidt-Kennicutt law and extinction that tracks gas density and enrichment. We find that the average IRX and SSFR follow a galaxy age parameter ξ, which is determined mainly by the galaxy mass and time since formation. We conclude that blue-sequence galaxies have properties which show simple, systematic trends with mass and time such as the steady buildup of heavy elements in the interstellar media of evolving galaxies and the exhaustion of gas in galaxies that are evolving off the blue sequence. The IRX represents a tool for selecting galaxies at various stages of evolution.

Subject headings: galaxies: evolution — ultraviolet: galaxies

1. INTRODUCTION

It has long been recognized that the present-day properties of most galaxies can be represented by relatively simple star formation histories (Tinsley 1968; Searle & Sargent 1972). While the physical basis for exponential star formation histories is almost certainly oversimplified, the resulting spectral energy distributions (SEDs) generally do an excellent job in representing galaxy spectra and broadband colors. If exponential models have a basis in the physics of star formation history, in particular in the conversion of gas into stars, then they make basic predictions that relate the specific star formation rate (SSFR) to the gas fraction in galaxies over time. Evidence for such a picture is growing (e.g., Bell et al. 2005; Noeske et al. 2007). Coupled with a model for chemical evolution, and brushing aside for the moment the complexities of dust reprocessing, this framework could also provide a description of the evolution of dust extinction in galaxies and the coevolution of extinction and star formation rate. In particular, we could expect a growth in the dust-to-gas ratio as gas is processed through stars and potentially an increase in extinction over time (e.g., as seen at $z \sim 2$ by Reddy et al. 2006). At the same time, as galaxies exhaust their gas supply, by whatever mechanism, we may detect a corresponding drop in extinction.

In order to discern such effects, we need to segregate galaxies by a parameter which is likely to be related to the timescale for evolution. There is certainly theoretical motivation for using stellar mass as the fundamental parameter. For example, surface density scales with stellar mass (Kauffmann et al. 2003), and star formation rate scales with gas surface density (Kennicutt 1989). The observational case for "downsizing" seems secure (Cowie et al. 1996; Brinchmann & Ellis 2000). The mass-metallicity relation (Tremonti et al. 2004) suggests that low metallicity in lower mass galaxies could be related to higher gas fractions and lower processing through star formation. Lower mass galaxies have younger stellar ages (e.g., Kauffmann et al. 2003). There is a well-known relationship between luminosity as a proxy for stellar mass and extinction (Wang & Heckman 1996) which is present even at high redshift (Meurer et al. 1999; Adelberger &

[1] California Institute of Technology, MC 405-47, 1200 East California Boulevard, Pasadena, CA 91125.
[2] Department of Astronomy, Columbia University, 528 West 120th Street, New York, NY 10027.
[3] Steward Observatory, University of Arizona, 933 North Cherry Avenue, Tucson, AZ 85721.
[4] Department of Physics, University of Oxford, Keble Road, Oxford OX1 3RHU, UK.
[5] Laboratory for Astronomy and Solar Physics, NASA Goddard Space Flight Center, Greenbelt, MD 20771.
[6] Space Sciences Laboratory, University of California at Berkeley, 601 Campbell Hall, Berkeley, CA 94720.
[7] Center for Astrophysical Sciences, The Johns Hopkins University, 3400 North Charles Street, Baltimore, MD 21218.
[8] Laboratoire d'Astrophysique de Marseille, BP 8, Traverse du Siphon, 13376 Marseille Cedex 12, France.
[9] Department of Physics and Astronomy, The Johns Hopkins University, Homewood Campus, Baltimore, MD 21218.
[10] Center for Space Astrophysics, Yonsei University, Seoul 120-749, Korea.
[11] Observatories of the Carnegie Institution of Washington, 813 Santa Barbara Street, Pasadena, CA 91101.
[12] Department of Physics and Astronomy, University of California, Los Angeles, CA 90095.
[13] Max-Planck-Institut für Astronomie, Konigstuhl 17, D-69117 Heidelberg, Germany.

Steidel 2000; Reddy et al. 2006; Papovich et al. 2006). We have recently established a tight relationship between metallicity and infrared excess (IRX), the ratio of far-infrared (FIR) to far-ultraviolet (FUV) luminosity (Johnson et al. 2007), that suggests that IRX may be used as a tracer of metallicity and its evolution. Finally, there is growing evidence that the so-called blue cloud of star-forming galaxies on the color-magnitude diagram (CMD) is actually a "blue sequence" in stellar mass (Wyder et al. 2007; Johnson et al. 2006) that is relatively tight in color space when extinction is corrected.

In order to distinguish trends with stellar mass, it is critical to have as large a mass dynamic range as possible. At the same time, dust extinction is likely to be a complex process that introduces considerable noise into any overall trends. Inclination variations alone produce much variance for an otherwise constant dust geometry and extinction law. We need to develop an approach which reveals the average trends with stellar mass in spite of this noise. A major benefit of a large multiwavelength survey is the ability to extract such trends by averaging over many galaxies. We have used *Spitzer* IRAC data to measure stellar mass and MIPS24 data for dust luminosity. We combine this with *GALEX* UV and COMBO-17 optical photometry and redshifts. A major difficulty we face when combining IR and UV survey data is the relatively small overlap in detected sources, with the bulk of the overlap occurring at high luminosity and mass. Thus, we have developed a new stacking approach which permits us to study the IRX over 2 orders of magnitude in stellar mass and over the redshift range $0.05 < z < 1.2$. Using this and a bolometric correction we obtain an average IRX over the UV, H-band CMD. We use this to find the total star formation rate, stellar mass, and SSFR. Finally, we show that the coevolution of the average IRX and SSFR can be modeled using simple exponential star formation histories and closed-box chemical evolution to $z \sim 1$.

We note that Zheng et al. (2007) have recently used an independent stacking technique (Zheng et al. 2006) to derive the SF history versus stellar mass, also using COMBO-17 and *Spitzer* data, and reached many conclusions that are similar to ours, although with important differences which we discuss in § 5.2.

We use a concordance cosmology $\Omega_\Lambda = 0.70$, $\Omega_m = 0.30$, and $H_0 = 70$ km s^{-1} Mpc^{-1}. We use AB magnitudes for all bands. We also use the following nomenclature: observed magnitudes are given by m_i, for example, the observed near-UV (NUV) and R magnitudes are $m_{\rm NUV}$ and m_R. Rest-frame magnitudes are denoted by FUV, NUV, H, etc. Extinction-corrected rest-frame absolute magnitudes are denoted $M_{\rm FUV,0}$, $M_{\rm NUV,0}$, $M_{H,0}$, etc. Finally, we define the infrared excess IRX as the log ratio of the FIR to the FUV luminosity ($\nu\mathcal{L}_\nu$), unless specifically called out.

2. DATA AND SOURCE CATALOGS

2.1. *Primary Data Sets*

2.1.1. *GALEX*

The *GALEX* observations of the Chandra Deep Field–South (CDF-S) consist of a total of 61 orbital visits over the period from 2005 November 4 to November 5 for a total exposure time of 49,758 s. Simultaneous exposures were obtained in the FUV (1344–1786 Å, with the center at 1549 Å) and NUV (1771–2831 Å, with the center at 2316 Å) bands. The individual and co-added images were processed using version 5.0 of the *GALEX* data pipeline, also used to process *GALEX* data releases GR2 and GR3. The 1.25° diameter *GALEX* images completely circumscribe the other two survey footprints. The *GALEX* mission, on-orbit performance, and current status of the calibration and pipeline reductions are summarized in Martin et al. (2005), Morrissey et al. (2005), and Morrissey et al. (2007), respectively. Source photometry errors (systematic) should be less than 0.05 mag, and astrometric errors less than 1″. Images of this exposure level in low background regions should reach a 5 σ Poisson-limited depth of $m_{\rm NUV} \simeq 25.5$ AB mag in both bands, and roughly 3 σ at $m_{\rm NUV} \simeq 26.0$. However, NUV data in particular are confusion-limited because of the 5″–6″ point-spread function (PSF) FWHM. We therefore used a PSF-fitting source-extraction procedure that uses the CDFS optical positions as priors. This is described below.

2.1.2. *COMBO-17*

The COMBO-17 survey (Wolf et al. 2003) combines a set of medium and wide photometric bands to obtain robust photometric redshifts and basic object classification to a depth of $m_R \sim 24$. A complete description of the survey can be found in Wolf et al. (2004). The CDFS field is 0.5×0.5 deg^2 centered on $(\alpha, \delta)_{\rm J2000.0} = (03^{\rm h}32^{\rm m}25^{\rm s}, -27°48'50'')$. Other than redshifts, we use the COMBO-17 survey for two purposes: to generate a k-corrected NUV luminosity and NUV $- H$ color, and as the basis for the PSF-fitting extraction of the FUV and NUV source fluxes. Wolf et al. (2004) have used a Monte Carlo technique to derive the survey completeness versus object color, type, and magnitude. We have used these completeness matrices to derive the volume-corrected distributions, as we describe below.

2.1.3. *Spitzer*

The *Spitzer* data are described in detail in Pérez-González et al. (2005), which we briefly recap here. The $1.5° \times 0.5°$ rectangular areas centered on CDFS, $(\alpha, \delta)_{\rm J2000.0} = (03^{\rm h}32^{\rm m}02^{\rm s}, -27°37'24'')$, are mapped with MIPS24 in scan-map mode, and also in the four IRAC channels (3.6, 4.5, 5.8, and 8.0 μm). The MIPS 24 μm reduction was performed using the MIPS Data Analysis Tool (Gordon et al. 2005), resulting in images with average exposures of ~1400 s. IRAC images were reduced with the general *Spitzer* pipeline and mosaicked, yielding an average exposure time of 500 s. Source catalogs for IRAC 3.6 μm detections are used below in a jointly selected sample. We tested catalogs generated by a simple one-pass SExtractor (Bertin & Arnouts 1996) extraction and by the multiband technique used by Pérez-González et al. (2005), with no significant differences noted in our results. Source catalogs of MIPS 24 μm objects were used to clean 24 μm images for stacking, as we describe below in § 3.3. Again, a single-pass SExtractor catalog produced very similar results to the multipass PSF-fitting catalog generated by Pérez-González et al. (2005).

2.2. *Matched Data Sets*

2.2.1. *GALEX/COMBO-17 PSF-Fitting Catalog*

As noted above, deep *GALEX* images suffer from source confusion, especially in the NUV. For fields with complementary deep optical photometry, we can use the positions of sources from the optical catalog to deblend the *GALEX* images and obtain more reliable flux estimates. The center of the COMBO-17 field is only slightly offset (3.8′) from the center of the *GALEX* images and is much smaller than the *GALEX* image. Within the COMBO-17 field, the variation of the *GALEX* PSF is small, and so we have used one average PSF for each band. After correcting for the small (less than 1″) systematic offsets between the *GALEX* and COMBO-17 astrometry, the deblending proceeds by dividing the region to be deblended into contiguous 100×100 pixel chunks and then simultaneously fitting the amplitudes of the sources at

TABLE 1
Source Detection and Matching Statistics

Bands	Number
$R < 24$	15,882
IRAC1 > 0.0005 mJy	13,754
MIPS24 > 0.02 mJy	3098
$R < 24$, NUV < 26.0	10,298
$R < 24$, NUV < 26.0, FUV < 26.0	4356
$R < 24$, IRAC1 > 0.0005	8196
$R < 24$, MIPS24 > 0.02	2090
$R < 24$, NUV < 26.0, MIPS24 > 0.02	1481
$R < 24$, NUV < 26.0, IRAC1 > 0.0005, MIPS24 > 0.02	1274

positions taken from the optical catalog and the mean background in each chunk. We assume that the counts in each pixel are Gaussian-distributed, which is a safe assumption for the NUV (where the background level is 100 counts) but is questionable for the FUV (where the background level is 10 counts). In order to test the reliability of our deblending, we have added approximately 1000 artificial point sources to the COMBO-17/*GALEX* overlap region and then compared the extracted fluxes with known input fluxes. In the FUV the deblended magnitudes are systematically fainter than the input magnitudes by 0.04 mag and have errors that are 20% larger than expected from counting statistics. In the NUV the deblended magnitudes are systematically too faint by only 0.01 mag, but the errors, due to the source crowding, are a factor of 2 larger than expected from counting statistics. For the 49,758 s *GALEX* images used here, the 95% confidence detection limits are 25.55 mag in the FUV and 25.10 mag in the NUV.

2.2.2. *Merged Catalog*

There is a low fraction of sources detected in all three catalogs. We generated individual source catalogs for the five *Spitzer* images using SExtractor. We matched these detections to the merged COMBO-17/*GALEX* catalog using a $2''$ search radius. The common area of the three surveys is 0.19 deg^2. The matched source statistics are summarized in Table 1. Of the 11,778 COMBO-17 $m_R < 24$ sources in the common region, 7498 are detected at $m_{\rm NUV} < 26$, 1784 with MIPS24 (>0.02 mJy), 4955 in NUV and IRAC1 (>0.0002 mJy), and 1171 in NUV, IRAC1, and MIPS24. As we discuss below, the main explanation for the low overlap fraction is that many UV-selected sources have moderate to low infrared-to-UV ratios and are not directly detected in the mid-infrared.

Because we are keenly interested in the evolution of the average extinction, IRX, and star formation history of galaxies over cosmic time, we have adopted a stacking approach. We summarize the complete methodology in the next section.

3. ANALYSIS

Our goal in this paper is to determine the evolution of the average IRX and extinction and relate this to the evolution of the star formation rate, as a function of stellar mass. We would like to exploit a property of the blue sequence of star-forming galaxies that is rapidly becoming clear: that this sequence has a relatively low dispersion of properties once the mass is given (Noeske et al. 2007; Wyder et al. 2007; Martin et al. 2007). The dispersion of various properties, such as extinction, stellar age, and mass, measured in individual bins of the NUV-*r* CMD, for example, is low. The IRAC1 channel and COMBO-17 *R* band give a good estimate of the rest-frame *H*-band flux over the redshift range $0 < z < 1.2$, providing a good stellar mass tracer with low extinction sensitivity. We therefore feel it is reasonable to stack using bins of the rest-frame (M_H, NUV $- H$) CMD.

3.1. *Methodology*

Here is a step-by-step summary of our approach, with cross-references to more detailed discussions:

1. Use COMBO-17 positions to generate a joint COMBO-17/*GALEX* catalog using PSF fitting (§ .2.1).
2. Match IRAC1 sources detected with SExtractor to the joint COMBO-17/*GALEX* catalog (§ 2.2.2).
3. Generate rest-frame NUV and *H*-band magnitudes using SED interpolation (§ 3.2).
4. Construct the volume-corrected CMD $\phi(M_H, {\rm NUV} - H)$ in several redshift bins (§ 3.2).
5. For each (M_H, NUV $- H$, z) bin, stack all IRAC2–4 and MIPS24 images at the *R*-band COMBO-17 source positions falling in that (M_H, NUV $- H$, z) bin. Our stacking technique adds detected source fluxes to a stack of undetected source regions, as we discuss in § 3.3.
6. Use a bolometric correction obtained by fitting a local SWIRE/SDSS/*GALEX* sample (Johnson et al. 2007) and the total FIR luminosity and infrared excess IRX $= \log \mathcal{L}_{\rm FIR}/\mathcal{L}_{\rm FUV}$ or $\log \mathcal{L}_{\rm FIR}/\mathcal{L}_{\rm NUV}$ (§ 3.3).
7. Use a standard extinction law to convert the IRX into NUV and *H*-band extinction (§ 3.4).
8. Determine the average extinction correction for galaxies in each (M_H, NUV $- H$, z) bin (§ 3.4).
9. Using $({\rm NUV} - H)_0$ and $M_{H,0}$ infer the SSFR and stellar mass using a simple prescription (§ 3.4).
10. Determine the volume-corrected distributions of specific star formation and stellar mass ($\mathcal{M}$) in each redshift bin $\phi(\mathcal{M}$, SSFR, $z)$ (§ 3.4).
11. Finally, calculate the average IRX and SSFR ($\langle {\rm IRX} \rangle$ and $\langle {\rm SSFR} \rangle$) as a function of stellar mass and redshift (§§ 4.3 and 4.4).

3.2. *Evolution of the Color-Magnitude Distribution*

We choose to use rest-frame FUV or NUV to derive the star formation rate and *H*-band magnitude to obtain stellar mass. Rest-frame *H*-band flux is obtained by interpolating between the COMBO-17 *R* magnitude and the IRAC 3.6 μm flux, exploiting the fact that the SED is essentially constant over this range for most galaxy templates. Rest-frame NUV flux is an interpolation of the observed NUV and the COMBO-17 catalog rest-frame *u*-band flux. Rest-frame FUV flux is an interpolation between the observed FUV and NUV, which accounts for the Lyman continuum break. We also tried SED fitting, which produces very similar results.

We derived the volume-corrected, rest-frame NUV $- H$ versus M_H distributions as follows. We used five redshift bins, $z =$ 0.05–0.2, 0.2–0.4, 0.4–0.6, 0.6–0.8, and 0.8–1.2. Maximum detection volumes were derived for a sample jointly selected in observed NUV, *r* band, and IRAC channel 1 with the following limits: $m_{\rm NUV} < 26.0$, $m_r < 24.0$, and $f(3.6) > 0.5$ μJy. The minimum $V_{\rm max}$ of the three bands was used. For each galaxy a completeness was calculated: $f_c = f_c({\rm NUV}) f_c({\rm C17})$. We assume that the IRAC channel 1 completeness is high to the flux limit. With PSF fitting, NUV completeness is estimated to be $\sim$80% at $m_{\rm NUV} = 25.5$ and $\sim$56% at $m_{\rm NUV} = 26.0$, based on comparison between the observed magnitude distribution and that measured by Gardner et al. (2000). Because of the soft roll-off of completeness for this PSF-fitting catalog, we choose to use a deeper magnitude cutoff corresponding to a 3 σ detection threshold. The

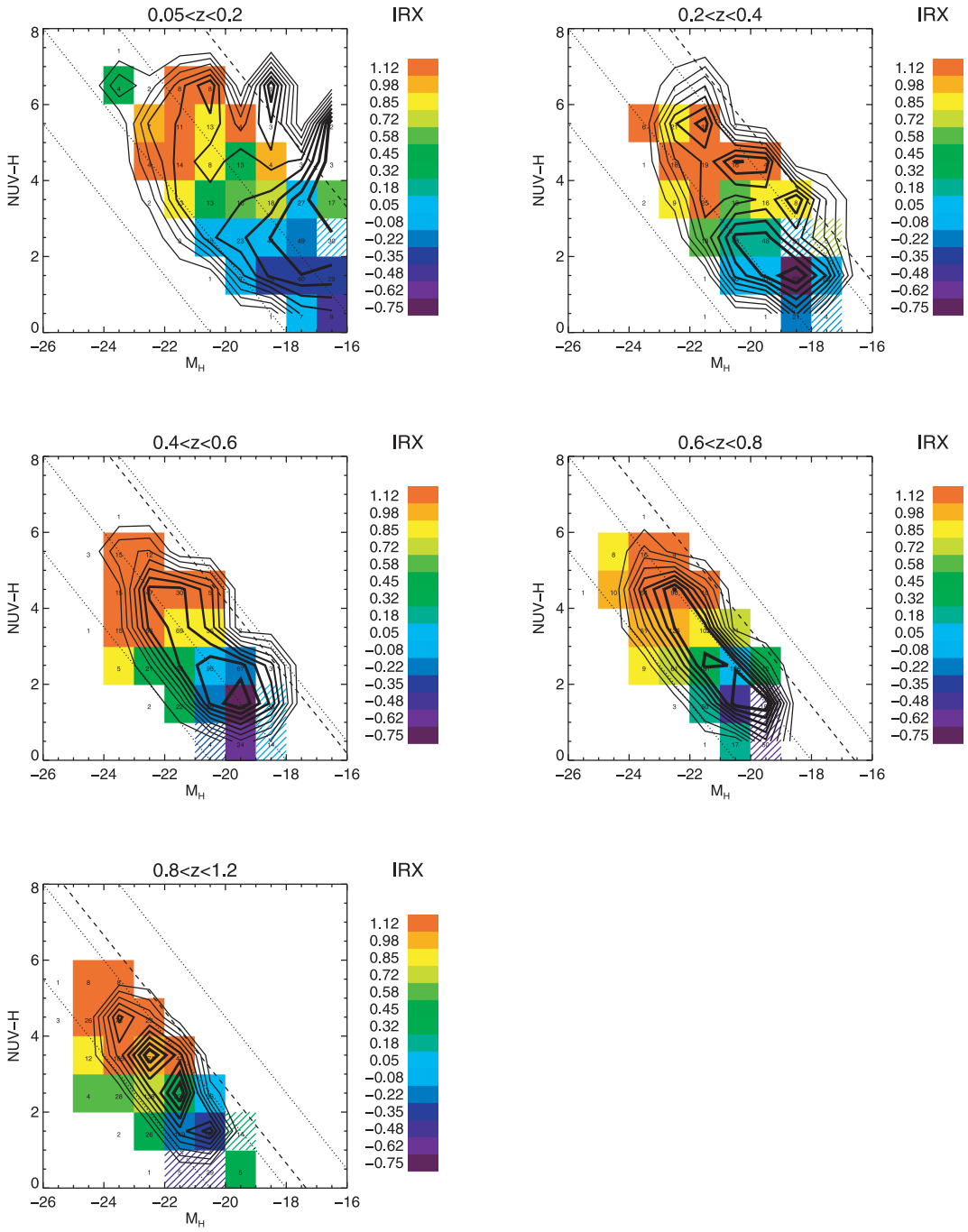

FIG. 1.—Volume-corrected, bivariate color-magnitude distribution $\phi(M_H, \mathrm{NUV} - H)$. Contours are equally spaced in log ϕ, with 10 divisions over $-4 < \log \phi < -2$. Colors give the IRX, which is the log of the FUV-to-FIR luminosity ratio. Hatched color bins show upper limits to the IRX. Dotted lines give loci of constant $M_{\mathrm{NUV}} = -15.5$, -18.0, and -20.5. Dashed diagonal lines indicate the $m_{\mathrm{NUV}} = 26$ limit in the center of the redshift bin.

COMBO-17 redshift catalog completeness is a function of object magnitude, color, and type. We use the completeness matrix derived by Wolf et al. (2003) to calculate f_c(C17) for each galaxy. The volume-corrected color-magnitude distribution is then calculated by summing for each galaxy the term

$$V_{\max,i} = \min[V_{\max}(\mathrm{NUV}_i, z_i), V_{\max}(r_i, z_i), V_{\max}(f(3.6)_i, z_i)] \times f_c(\mathrm{NUV}_i) f_c(r_i; g_i - r_i), \quad (1)$$

$$\phi(\mathrm{NUV} - H, M_H, z) = \sum \frac{1}{V_{\max,i}}. \quad (2)$$

The resulting distribution is displayed in contour plots in Figure 1. The general trend that can be seen is a shift to bluer NUV $-$ H colors and brighter M_H magnitudes. These plots also show the average IRX in each bin, to be discussed in the next section.

3.3. *IR Stacking, Bolometric Correction, and Extinction Correction*

We have generated an average IRX for each bin in the (M_H, NUV $-$ H) CMD. As we discussed earlier, we do this because of the small overlap in UV and MIPS detections. There is considerable

TABLE 2
Bolometric Correction Coefficients

λ	a_λ	b_λ
12	0.710	0.037
13	0.705	0.036
14	0.778	0.033
15	0.860	0.030
16	0.884	0.026
17	0.878	0.023
18	0.874	0.020
19	0.880	0.016
20	0.874	0.011
21	0.873	0.007
22	0.863	0.003
23	0.854	0.000
24	0.824	−0.004

Note.—Where $\log \mathcal{L}_{\rm FIR} = a_\lambda + b_\lambda \log(\mathcal{L}[\lambda]/10^{10}\ \mathcal{L}_\odot)$.

evidence that galaxies occupying a single color-magnitude bin have a relatively small dispersion in most properties, including extinction (Martin et al. 2007; Wyder et al. 2007; Johnson et al. 2006). This approach allows us to estimate the average IRX over a large range of stellar mass and redshift, offering sensitivity to quite low IRX. In order to ensure that the technique is not affected by systematic or random error, we perform a set of tests below.

The basic stacking technique is as follows. We first generate a catalog of detected sources in the MIPS 24 μm band using SExtractor. Using this catalog we generate a set of cleaned images with detected sources removed. For each redshift and each color-magnitude bin (NUV $-$ H, M_H, z) we stack images in each band that do not have detected sources. We then extract either a source flux or an upper limit, and add this to the detected flux. This results in a flux or upper limit.

We must then make a bolometric correction to the observed 24 μm luminosity. We have used the *GALEX*/SWIRE catalog generated for Johnson et al. (2006, 2007) to derive the bolometric correction of the rest-frame flux from 12 to 24 μm (corresponding to $0 < z < 1$). We use the measured FIR fluxes and fits to Dale & Helou (2002) SEDs and derive coefficients in the following relationship using log-log fits:

$$\log \mathcal{L}_{\rm FIR} = a_\lambda + b_\lambda \log\bigl(\mathcal{L}[\lambda]/10^{10}\ \mathcal{L}_\odot\bigr), \tag{3}$$

where λ is the observed rest-frame luminosity ($\mathcal{L}[\lambda] = \nu\mathcal{L}_\nu[\lambda]$). We list in Table 2 the coefficients a_λ and b_λ. The rms errors in the fits used to derive the coefficients are small: $\sigma \simeq 0.03$–0.06.

Finally, we correct the NUV $-$ H color and H-band magnitude for internal extinction using the IRX and the following prescription based on Calzetti et al. (2000):

$$A_i = 2.5 \log\left(\frac{\rm BC_{dust}}{\rm BC_{\it i}} {\rm IRX}_i + 1\right), \tag{4}$$

where i corresponds to either the FUV or NUV and the bolometric corrections are $\rm BC_{dust} = 1.75$, $\rm BC_{FUV} = 1.68$, and $\rm BC_{NUV} = 2.45$.

Since the H-band correction is small, the extinction correction is very insensitive to the extinction law. It enters somewhat if we use $\mathcal{L}$(FUV) to generate $\rm IRX_{FUV}$ and use this to correct (NUV $-$ H). Even if there is evolution in the extinction law, we have found that using $\rm IRX_{NUV}$ gives very similar results to those using $\rm IRX_{FUV}$. The volume-corrected distribution of extinction-corrected magnitudes $\phi(M_{H0}, [{\rm NUV} - H]_0)$ versus redshift are given in Figure 2. We show in Figure 3 the uncorrected and corrected distribution in NUV $-$ H.

3.4. *Stellar Mass and Specific Star Formation Rate*

We derive the stellar mass $\mathcal{M}$ using the extinction-corrected rest-frame H-band absolute magnitude and NUV $-$ H color, following the basic scheme of Bell et al. (2003). For smooth star formation histories the stellar mass-to-light ratio is a single parameter function of a measure of the SSFR such as the rest-frame extinction-corrected NUV $-$ H color. This can be seen in Figure 4, which shows the predicted $\mathcal{M}/\mathcal{L}$ versus $({\rm NUV} - H)_0$ for different values of the exponential SFR decay, based on solar-metallicity models of Bruzual & Charlot (2003) and a (standard, nondiet) Salpeter initial mass function.[14] There is almost no dependence on the star formation history for $({\rm NUV} - H)_0$ for NUV $-$ $H < 2.5$, where the bulk of the extinction-corrected galaxies fall. We use this parabolic fit:

$$\log\left(\frac{\mathcal{M}}{\mathcal{L}}\right) = -0.667 + 0.17({\rm NUV} - H)_0 + 0.00373({\rm NUV} - H)_0^2. \tag{5}$$

We have also tested more complex star formation histories in which starbursts become significant. These models produce the same general trends between $\mathcal{M}/\mathcal{L}$ and NUV $-$ H color, with some dispersion. There is no significant impact on the results described below.

We derive the star formation rate from the extinction-corrected FUV luminosity using ${\rm SFR} = 1.4 \times 10^{-28} \mathcal{L}_\nu(1500)$ (Kennicutt 1998). We obtain the SSFR by dividing by the stellar mass.

We also note that the SSFR is tightly correlated with $({\rm NUV} - H)_0$ and independent of decay timescale, as can be seen in Figure 4. We can also use the following linear fit to convert $({\rm NUV} - H)_0$ to SSFR:

$$\log\bigl({\rm SSFR}\bigl[{\rm yr}^{-1}\bigr]\bigr) = -7.8 - 0.65({\rm NUV} - H)_0. \tag{6}$$

Again, either technique for computing the SSFR produces essentially identical results.

We derive the stellar mass and SSFR for each galaxy by correcting its rest-frame M_H, M_{1500}, and NUV $-$ H for the (bin-averaged) extinction. Using these distributions we derive the volume-corrected bivariate $\mathcal{M}$-SSFR distribution $\phi(\mathcal{M}, {\rm SSFR}, z)$ in the same fashion as for the volume-corrected color-magnitude distribution. We also generate an average IRX in each bin of the $\mathcal{M}$-SSFR distribution. We calculate the mean log IRX in each bin, using the IRX obtained in the previous section. These distributions are displayed in Figure 5.

3.5. *Errors*

We use the bootstrap method (Efron 1979) to derive errors to all bivariate distributions discussed above, as well as to the average distributions discussed in the next section. Specifically, in each redshift bin we randomly select objects, with replacement, until we have the same number of objects found in that redshift bin. We then proceed to determine the color-magnitude distribution, the mean 24 μm flux in each color-magnitude bin by

[14] Note that all derived stellar masses and star formation rates can be converted to the "Diet Salpeter" IMF of Bell et al. (2003) by multiplying by 0.7. SSFRs are unaffected.

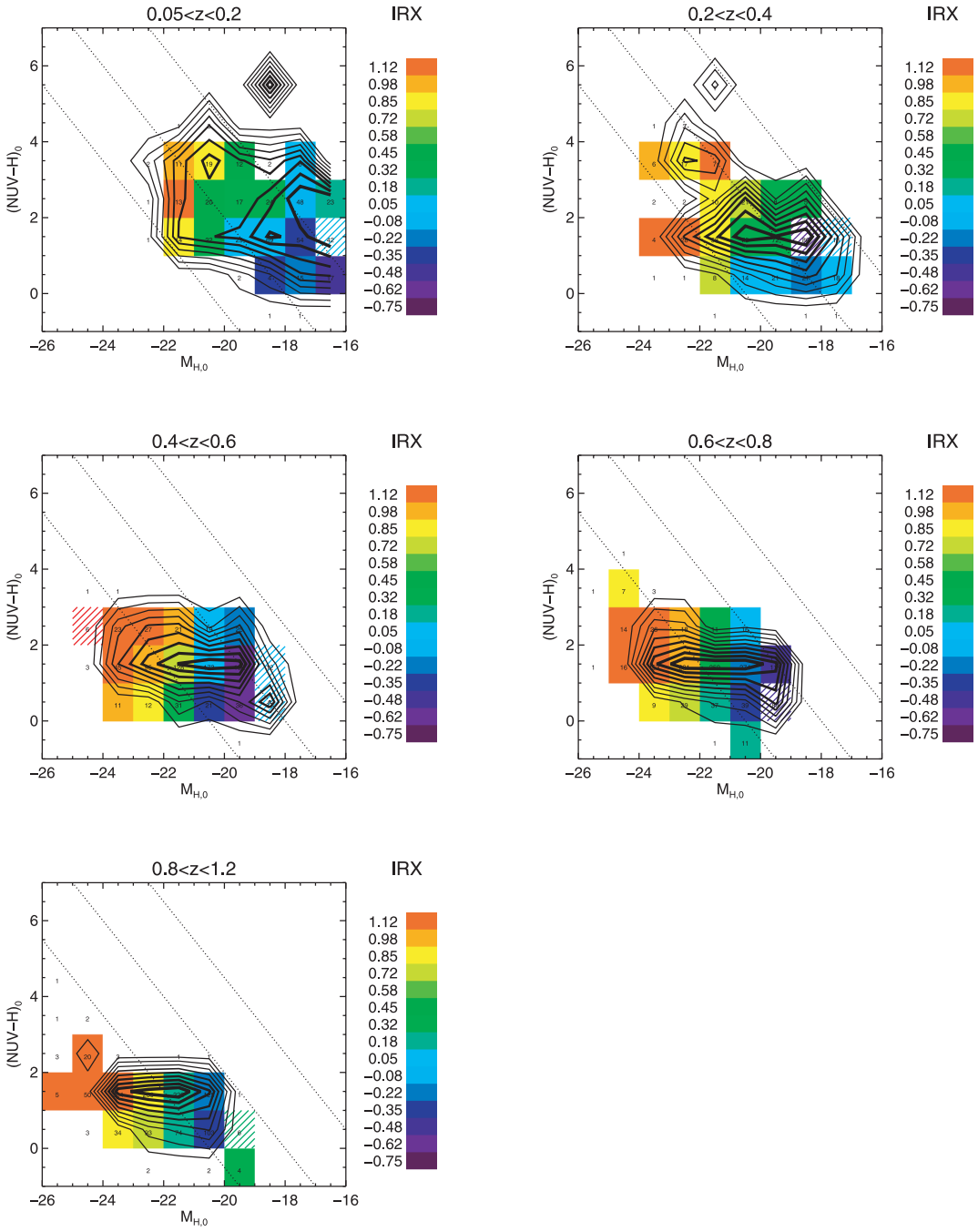

FIG. 2.—Volume-corrected, bivariate, *extinction-corrected* color-magnitude distribution $\phi(M_{H,0}, (\mathrm{NUV} - H)_0)$. Contours are equally spaced in $\log \phi[\mathrm{Mpc}^{-3}]$, with 10 divisions over $-4 < \log \phi < -2$. Colors give the IRX, which is the log of the FUV-to-FIR luminosity ratio. Hatched color bins show upper limits to the IRX. Dotted lines give loci of constant $M_{\mathrm{NUV},0} = -15.5, -18.0$, and -20.5.

stacking this new sample, the corrected CMD, the mass-SSFR distribution, and the mean IRX in each mass-SSFR bin (see § 4.3). Of order 100 trials are used to generate a standard deviation in each bin of every distribution calculated. Such errors will not, however, account for cosmic variance due to large-scale structure. (see § 5.2).

4. RESULTS

4.1. *Infrared Excess versus Stellar Mass*

We begin by examining the trends in the $(\mathrm{NUV} - H, M_H)$ CMD. At a fixed M_H redder galaxies have a higher IRX. In general, the blue sequence shows a significant tilt in the CMD, much of which appears to be produced by this extinction-luminosity relationship. Much of the color width of the blue sequence, which leads some authors to refer to it as the "blue cloud," is also produced by variance in extinction (Wyder et al. 2007), some of which is simply due to inclination variations (Martin et al. 2007). Extinction correction produces a much tighter distribution in the CMD, as we see in Figures 2 and 3. The trend of increasing IRX with H-band luminosity is even more apparent in the extinction-corrected CMD. Consequently, there is a strong increase in IRX with stellar mass, as is expected from the trend in the CMD. This trend can be clearly detected in Figure 5. This trend persists in all redshift bins.

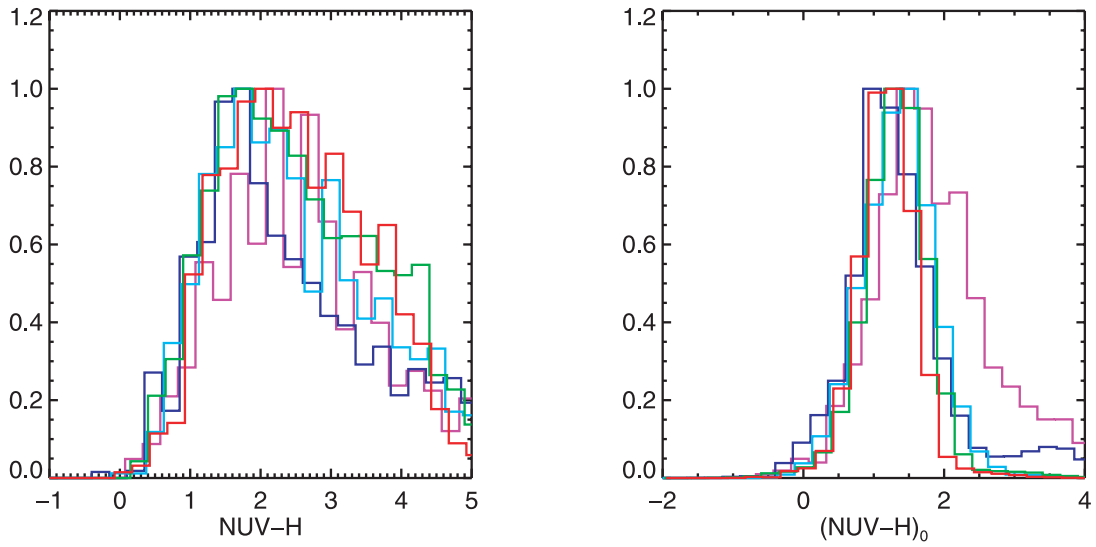

FIG. 3.—Distribution of the observed NUV − H (*left*) and extinction-corrected $(\mathrm{NUV} - H)_0$ (*right*). Color gives the redshift bin: $0.05 < z < 0.2$ (*purple*), $0.2 < z < 0.4$ (*blue*), $0.4 < z < 0.6$ (*cyan*), $0.6 < z < 0.8$ (*green*), and $0.8 < z < 1.2$ (*red*).

4.2. *Evolution of the Bivariate CMD*

There is clear evolution in the $(\mathrm{NUV} - H, M_H)$ CMD, in the sense that the density of H-band-luminous galaxies is increasing with redshift. This is consistent with the increase in characteristic UV luminosity (Schiminovich et al. 2005) and B luminosity (Bell et al. 2004). As expected from the previous section, this is accompanied by an increase in the contribution from higher IRX galaxies. The evolutionary trend is even easier to discern in the extinction-corrected CMD in Figure 2.

4.3. *Infrared Excess versus Stellar Mass and Redshift*

In order to further explore the IRX-mass relationship and its evolution we derive the average IRX in each mass and redshift bin. We have calculated this average using the number density $\langle \mathrm{IRX} \rangle(\mathcal{M})$ and weighted by the star formation rate $\langle \mathrm{IRX} \rangle_{\mathrm{SFR}}(\mathcal{M})$. The mass trend in redshift bins is shown in Figure 6. The average IRX increases sharply with mass up to a critical mass. The slope in the IRX–log mass relation is greater than 1. The critical mass is lower at low redshift, $\simeq$10.5 at $z \sim 0.3$, but appears to move to higher mass at higher redshift, with $\sim$11.5 at $z \sim 1$.

The redshift trend in mass bins is shown in Figure 7. In the highest mass bin with good redshift coverage ($\log \mathcal{M}_{\mathrm{crit}} = 11.5$), IRX increases slowly with time then sharply decreases for $z < 0.5$. In the lowest mass bin, IRX appears to increase with time to the lowest redshift bin. These trends appear in both the number- and SFR-weighted average IRX. For our subsequent analysis we use the number-weighted average.

4.4. *Coevolution of SFR and IRX*

We have seen that the star formation rate density is moving to higher masses at higher redshift. This can best be seen in the SFR-weighted bivariate $\mathcal{M}$-SSFR distributions shown in Figure 8. It is interesting to determine the average SSFR versus mass and redshift as we did for IRX. The number-averaged SSFR is given in Figure 9. This shows that at lower masses, $\log \mathcal{M} = 9.5$, $\langle \mathrm{SSFR} \rangle$ evolves slowly, while at higher masses the SSFR falls rapidly with time.

The behavior in Figures 6, 7, and 9 can be explained by a simple model. We suppose that the average IRX is determined principally by the gas surface density and by the metallicity. This naturally produces a rising then falling IRX as the gas becomes enriched (in a closed-box model) and then exhausted. Downsizing implies that star formation, enrichment, and ultimate gas exhaustion move to lower masses with time, consistent with these results.

We examine this model further in the next section. But first we ask whether the observed trends could be an artifact of selection effects or other aspects of our technique.

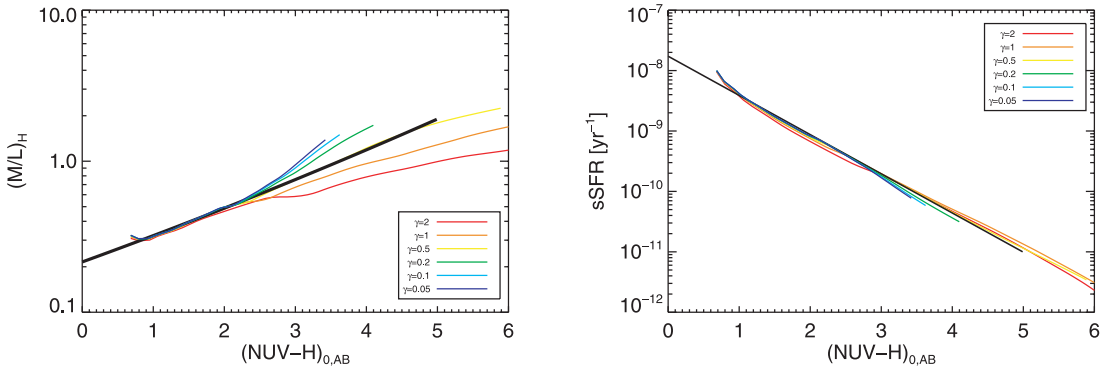

FIG. 4.—*Left*: Mass-to-light ratio at H band vs. $(\mathrm{NUV} - H)$ for exponentially declining star formation histories $e^{-\gamma t}$, obtained using the model of Bruzual & Charlot (2003). *Right*: SSFR for exponentially declining star formation histories.

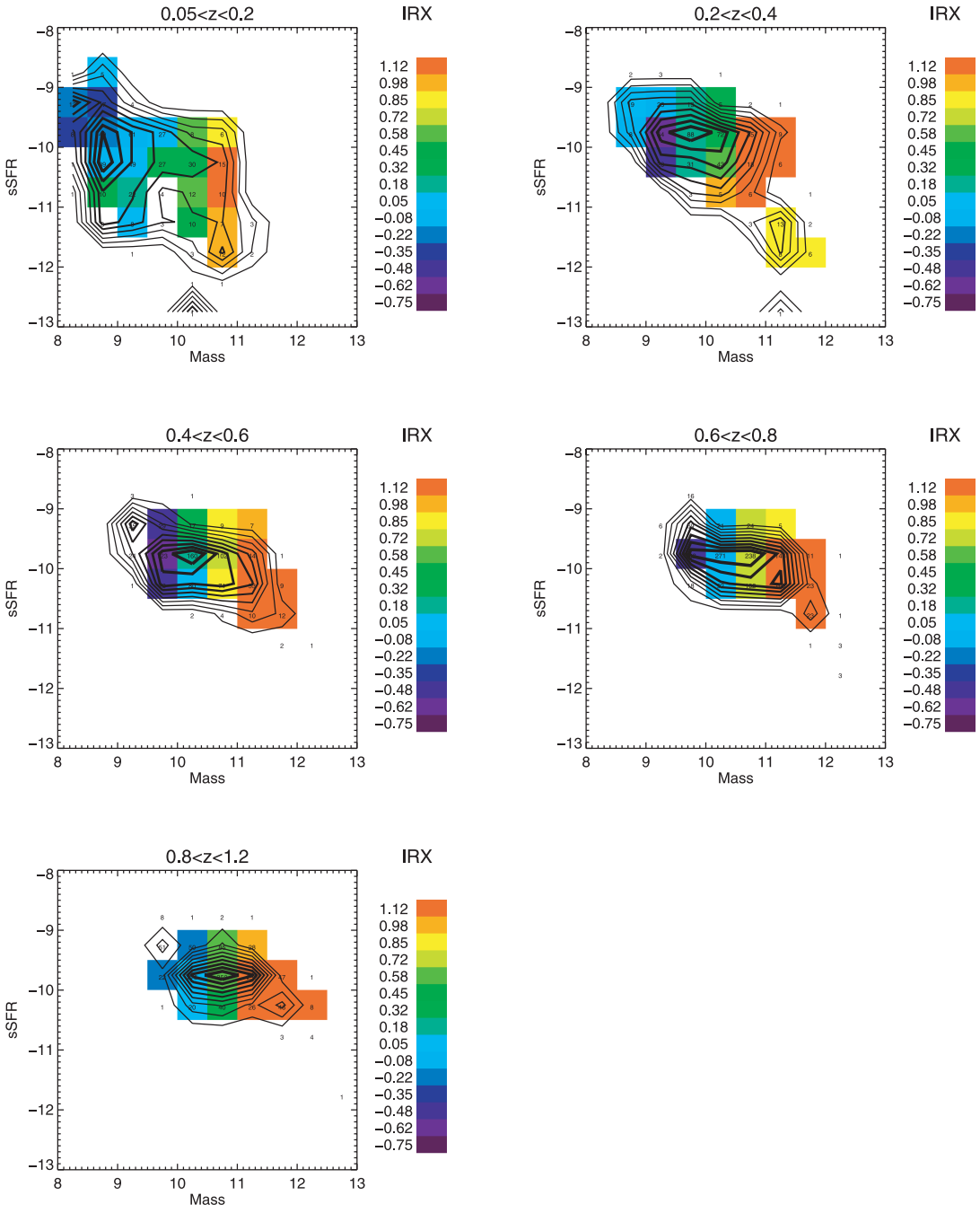

FIG. 5.—Volume-corrected, bivariate mass-SSFR distribution $\phi(\mathcal{M}, \mathrm{SSFR})$. Contours are equally spaced in $\log \phi[\mathrm{Mpc}^{-3}]$, with 10 divisions over $-4 < \log \phi < -1$. Colors give the IRX, which is the log of the FUV-to-FIR luminosity ratio.

4.5. *Issues and Caveats*

We have performed a number of tests to ensure that the results presented above are not a product of the samples or analysis approach.

We could use either FUV (1530 Å) or NUV (2270 Å) flux to derive star formation rates. Since we bin and stack sources in the NUV-*H* CMD, either there could be systematic effects introduced by the use of an extinction law to correct the FUV given the NUV-derived IRX, or there could be effects introduced by the different data samples used to derive the FUV and NUV rest-frame luminosities. The former come completely from *GALEX* data, while the latter come from interpolating *GALEX* and COMBO-17 data. We find, however, that there is no significant difference in the results using FUV or NUV to derive IRX and SFR.

We tested stacking the MIPS24 data using detected sources and cleaned images, and using only the fluxed images (stacking detected and undetected sources together). This produced no statistically significant difference. We also were concerned about the MIPS24 detection limit and whether the low limit of 0.02 mJy used to detect and clean the images would include some spuriously detected sources due to confusion, yielding an artificially high 24 μm flux in the stacked result. We checked this by increasing the detection limit by a factor of 2 and repeating the entire analysis. Again, these results showed only minor quantitative changes.

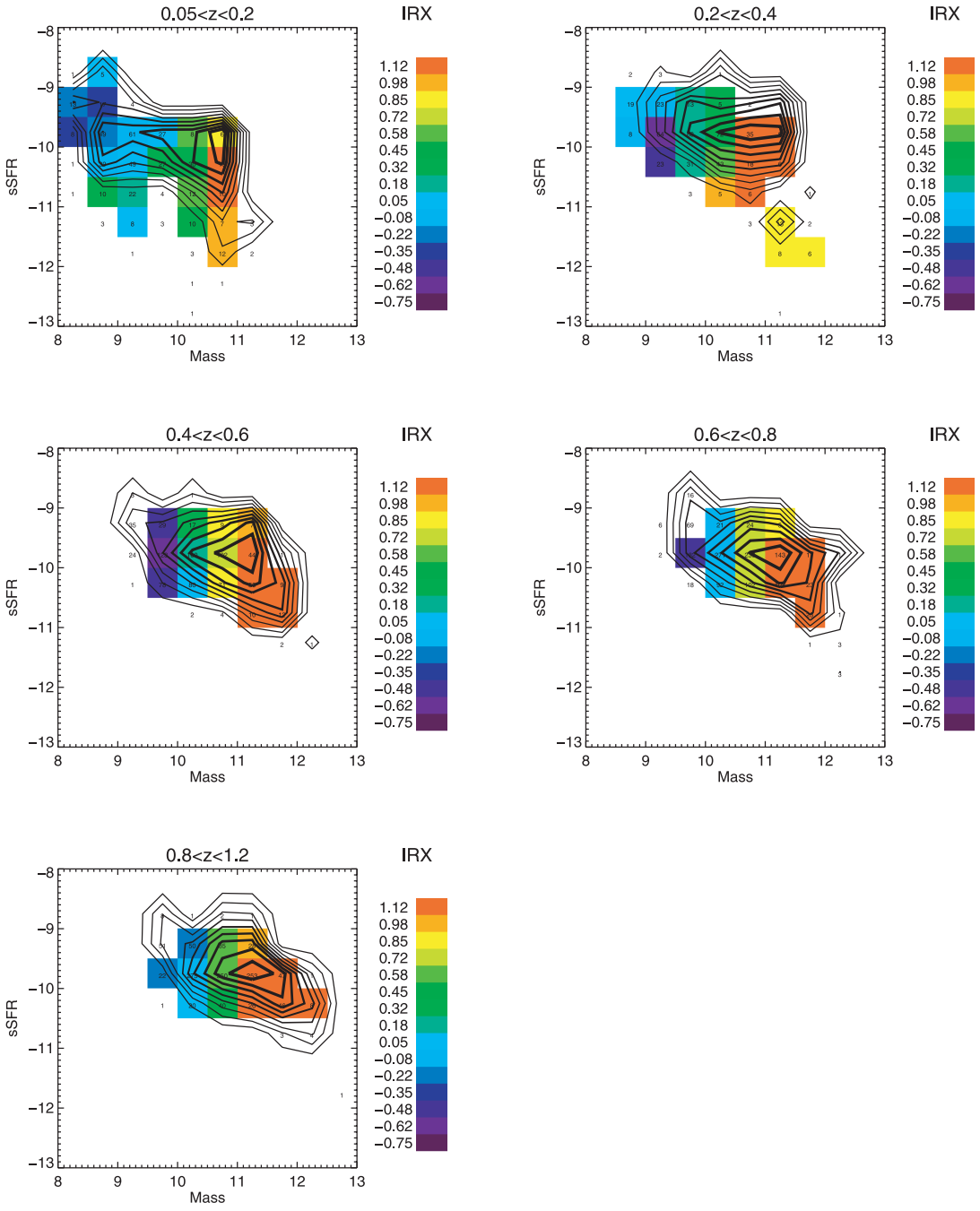

FIG. 6.—Volume-corrected, bivariate mass-SSFR distribution weighted by the SFR: SFR $\times \phi(\mathcal{M}, \mathrm{SSFR})$. Contours are equally spaced in $(\log \mathrm{SFR})\phi$ [$\mathcal{M}_{\odot}$ yr^{-1} Mpc^{-3}], with 10 divisions over $-4 < (\log \mathrm{SFR})\phi < -1$. Colors give the IRX, which is the log of the FUV-to-FIR luminosity ratio.

A very important question is whether our census of objects is complete. We could be missing FIR-luminous objects that fall below the UV magnitude limits of the sample. Moreover, it is likely that as we move to higher redshift, more of the high IRX and/or low SSFR sources are lost due to the UV magnitude limit. This could clearly introduce a spurious blueing trend as redshift increases, which is exactly what we detect.

To test for this effect, we repeated the analysis on the following samples: (1) baseline: NUV < 26.0 and $r < 24.0$; (2) case 2: NUV < 25.0 and $r < 24.0$; (3) case 3: NUV < 27.0 and $r < 24.0$; (4) case 4: NUV < 26.0 and $r < 25.0$; (5) case 5: all $r < 24.0$ objects, whether or not detected in NUV. Those objects below the NUV detection limit are given an artificial magnitude NUV $= 27.0$. The average IRX versus redshift for these cases is shown in Figure 10. There are no significant changes to $\langle \mathrm{IRX} \rangle$ or in the observed trends with mass and redshift.

Another test is to consider the inclination bias of the sample. A sample at high redshift which has not included highly inclined, more reddened galaxies of otherwise similar overall dust content will display a higher average minor-to-major axis ratio than the low-redshift counterpart. The average axis ratio obtained from the (seeing-limited) COMBO-17 data shows no significant trends with redshift. This is true in the (M_H, NUV-H) CMD and, as we show in Figure 11, the final $\mathcal{M}$-SSFR diagram.

Finally, we used a Monte Carlo model to test whether the evolving IRX-mass relationship could be an artifact of the sample

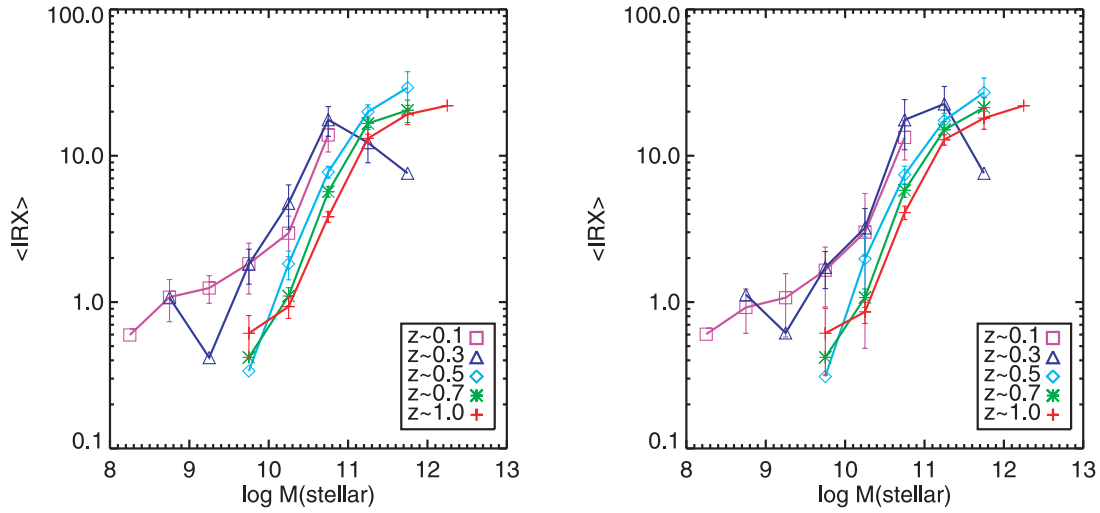

FIG. 7.—Average IRX ($\langle$IRX$\rangle$; linear version plotted on a logarithmic scale) vs. mass in each redshift bin. *Left*, Numerical average; *right*, SFR-weighted average. Errors are derived from bootstrapping.

selection. The model is semiempirical, and we briefly summarize it here. The model predicts the bivariate luminosity function in the extincted, rest-frame (NUV $-$ H, M_H) CMD, and the distribution of $\langle$IRX$\rangle$ over the same CMD ($\langle$IRX$\rangle[M_H, \mathrm{NUV} - H]$). The number distribution is given by a Schechter function in mass. The SSFR is lognormal with a constant mean and variance to a certain critical mass, then falls. The IRX is lognormal, and the mean IRX scales with mass. Evolution is introduced into the number density, mean SSFR, SFR cutoff mass, and IRX-mass relationship. In the latter case the following relationship is introduced:

$$\mathrm{IRX} = \mathrm{IRX}_0 + a_m\left(\log\frac{\mathcal{M}}{\mathcal{M}_0}\right) + a_{m,z}\left(\log\frac{\mathcal{M}}{\mathcal{M}_0}\right)\log(1+z) + \sigma_{\mathrm{IRX}}\xi, \tag{7}$$

where ξ is a normally distributed random variable. This assumption allows for IRX dependence on mass, and evolution of this dependence in a mass-dependent fashion: in other words the evolutionary trends we appear to detect in the data.

We convert mass, SSFR, and IRX into the observed SEDs using (in reverse) the identical transformations that we used for the data. The SEDs are redshifted and run through detection filters with appropriate completeness functions. We then subject the list of objects and observed FUV, NUV, *R*-band, IRAC, and MIPS24 fluxes to analysis steps identical to those for the actual sources, producing the various distributions. (We do not simulate the actual image formation and detection process). Finally, we compare the Monte Carlo and data distributions using a χ^2 statistic. For this comparison we combine data and Monte Carlo errors (data errors calculated from bootstrap and Monte Carlo errors calculated from Poisson statistics). To calculate χ^2 we use all bins in which either data exist or Monte Carlo results are predicted. We simultaneously fit both $\phi(M_H, \mathrm{NUV}-H)$ and $\langle\mathrm{IRX}\rangle(M_H, \mathrm{NUV} - H)$ over all five redshift bins.

Because the model has ~10–14 parameters, it is difficult to guarantee that any given local minimum is the global minimum. Extensive experimentation has shown that the ϕ-distribution and IRX distributions are mainly influenced by separate variables, so some minimization can be decoupled. We find best fits with $a_{m,z} \simeq 1.5$ and $a_m \simeq 0.3$, with $\log \mathcal{M}_0 \simeq 11.0$ and with small formal errors (<0.05). The latter are derived in the usual way by fixing the parameter of interest and marginalizing over

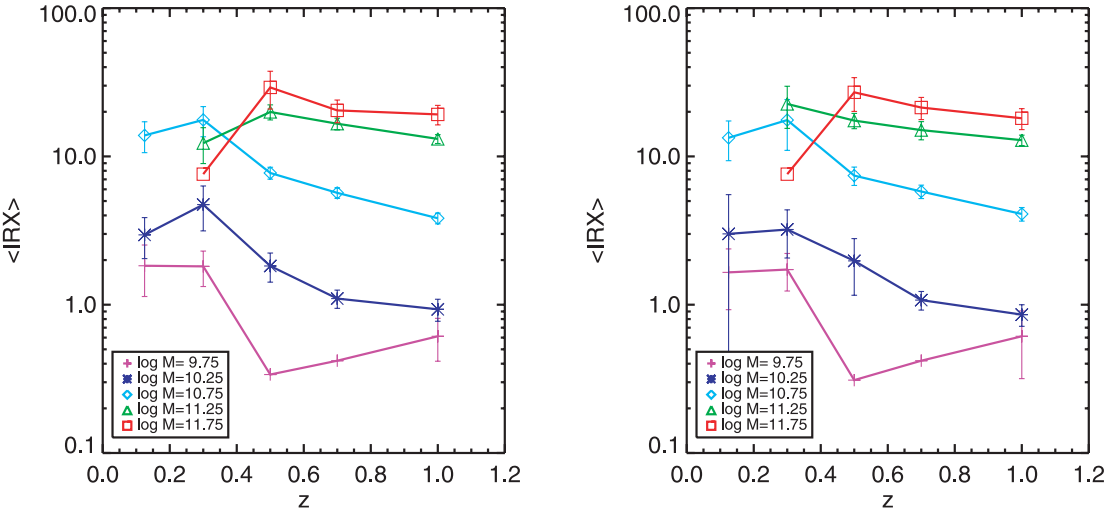

FIG. 8.—Average IRX ($\langle$IRX$\rangle$; linear version plotted on a logarithmic scale) vs. redshift in each mass bin. *Left*, numerical average; *right*, SFR-weighted average. Errors are derived from bootstrapping.

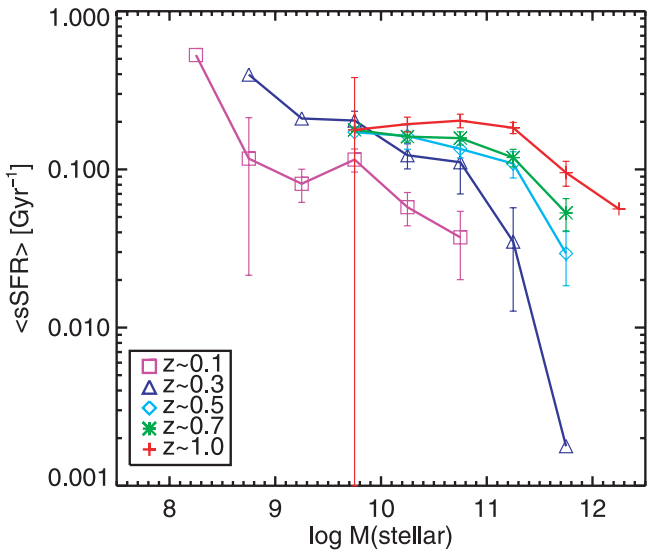

FIG. 9.—Average SSFR ($\langle$SSFR$\rangle$) in each mass and redshift bin. Errors are derived from bootstrapping.

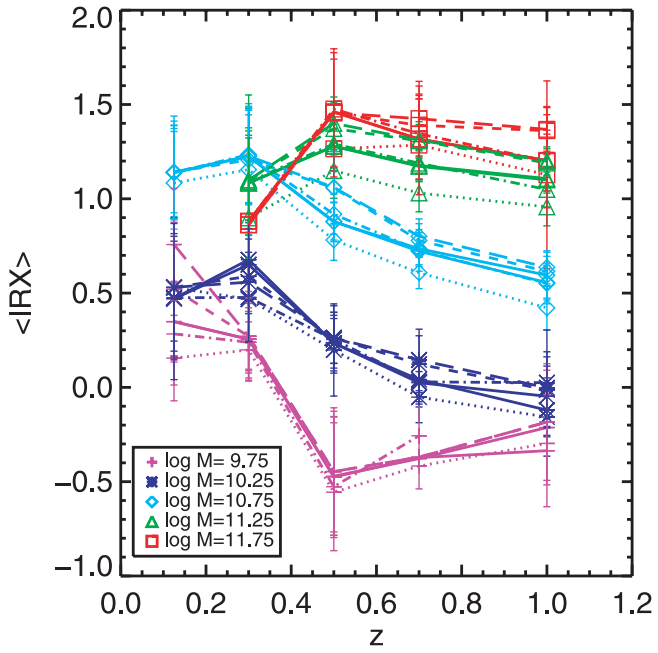

FIG. 10.—Average IRX ($\langle$IRX$\rangle$) vs. redshift in each mass bin using various techniques as indicated by line styles: baseline (NUV < 26.0, $r < 24.0$; *solid line*); case 2 (NUV < 25.0, $r < 24.0$; *dotted line*); case 3 (NUV < 27.0, $r < 24.0$; *dashed line*); case 4 (NUV < 26.0, $r < 25.0$; *dash-dotted line*); case 5 (all $r < 24.0$ objects, whether or not detected in NUV; *dash-double-dotted line*).

all others. The key conclusion is that the significant nonzero value of $a_{m,z}$ provides additional evidence that the evolving IRX-mass relationship is not an artifact of the sample selection.

5. DISCUSSION

5.1. *Simple Extinction, Metallicity, and Star Formation Evolution*

The phenomena displayed in Figures 6 and 7 have a very simple interpretation. At low mass, ongoing enrichment by star formation increases the dust-to-gas ratio and mean extinction per unit gas, resulting in a steady growth in the IRX. Higher mass galaxies had their periods of peak star formation in the past, and the exhaustion of their star-forming gas supply (by whatever mechanism) leads to an IRX which falls with time. We reiterate that our determination of the IRX is obtained directly from the FUV-to-FIR ratio (the latter from 12 to 24 μm luminosity and a bolometric correction) and is independent of the extinction law.

We can model this using the classical exponential SFR models introduced by Tinsley (1968) and a very simple extinction model. The SFR obeys

$$\mathrm{SFR} \sim e^{-(t-t_0)/\tau} = e^{-\xi}, \tag{8}$$

where ξ is a scale-free "age" parameter.

For simplicity, we characterize the extinction as if it occurs in a simple foreground absorbing slab of dust, and that its strength tracks the amount of gas responsible for star formation:

$$A_{\mathrm{FUV}} \sim Z\Sigma_{\mathrm{gas}}, \tag{9}$$

where Z is the metallicity (we assume that the gas-to-dust ratio scales accordingly) and Σ_{gas} is the gas surface density. Ignoring inclination-induced anisotropies, we have IRX $=$ $\log(10^{(0.4A_{\mathrm{FUV}})} - 1)$. Let us further assume a Schmidt-Kennicutt scaling law (Kennicutt 1989), SFR $\sim \Sigma_{\mathrm{gas}}^{\beta}$. Here we note $\beta \simeq 1.5$. Then

$$\Sigma_{\mathrm{gas}} \sim e^{-\xi/\beta}. \tag{10}$$

In a closed-box enrichment model, metallicity grows as

$$Z = y \ln \mu_{\mathrm{gas}}^{-1} = y\xi \tag{11}$$

for an exponentially decaying SFR. The gas fraction is μ_{gas}, and y is the average yield (Searle & Sargent 1972). Thus, we expect

$$A_{\mathrm{FUV}} = C_0 \xi e^{-\xi/\beta}. \tag{12}$$

Here C_0 is a scaling constant appropriate for an average inclination.

This can be generalized to the leaky-box case (Hartwick 1976) in which the outflow is proportional to the star formation rate $\mathcal{M}_{\mathrm{wind}} = -c \times \mathrm{SFR}$. In this case

$$Z = \frac{y}{1+c} \ln \mu_{\mathrm{gas}}^{-1} = \frac{y}{1+c}\xi. \tag{13}$$

If $c < 1$ then an accreting-box case (Binney & Merrifield 1998) with infall proportional to SFR would obtain. We do not consider other accreting-box scenarios.

Finally, we need to relate the age parameter to galaxy mass.[15] We make a simple *Ansatz* that the age scales as mass to a constant power α, that a single formation time t_f is appropriate, and that the past age is reduced by the relative elapsed time from formation:

$$\xi(\mathcal{M}, z) = \left(\frac{\mathcal{M}}{\mathcal{M}_0}\right)^{\alpha} \left[\frac{t(z) - t_f}{t(0) - t_f}\right]. \tag{14}$$

[15] We label galaxies by their stellar mass. Over the redshift range we consider, a constant SFR would increase the stellar mass by 0.5 dex, or one mass bin. We ignore this subtlety in order to make the arithmetic simple for this very basic model.

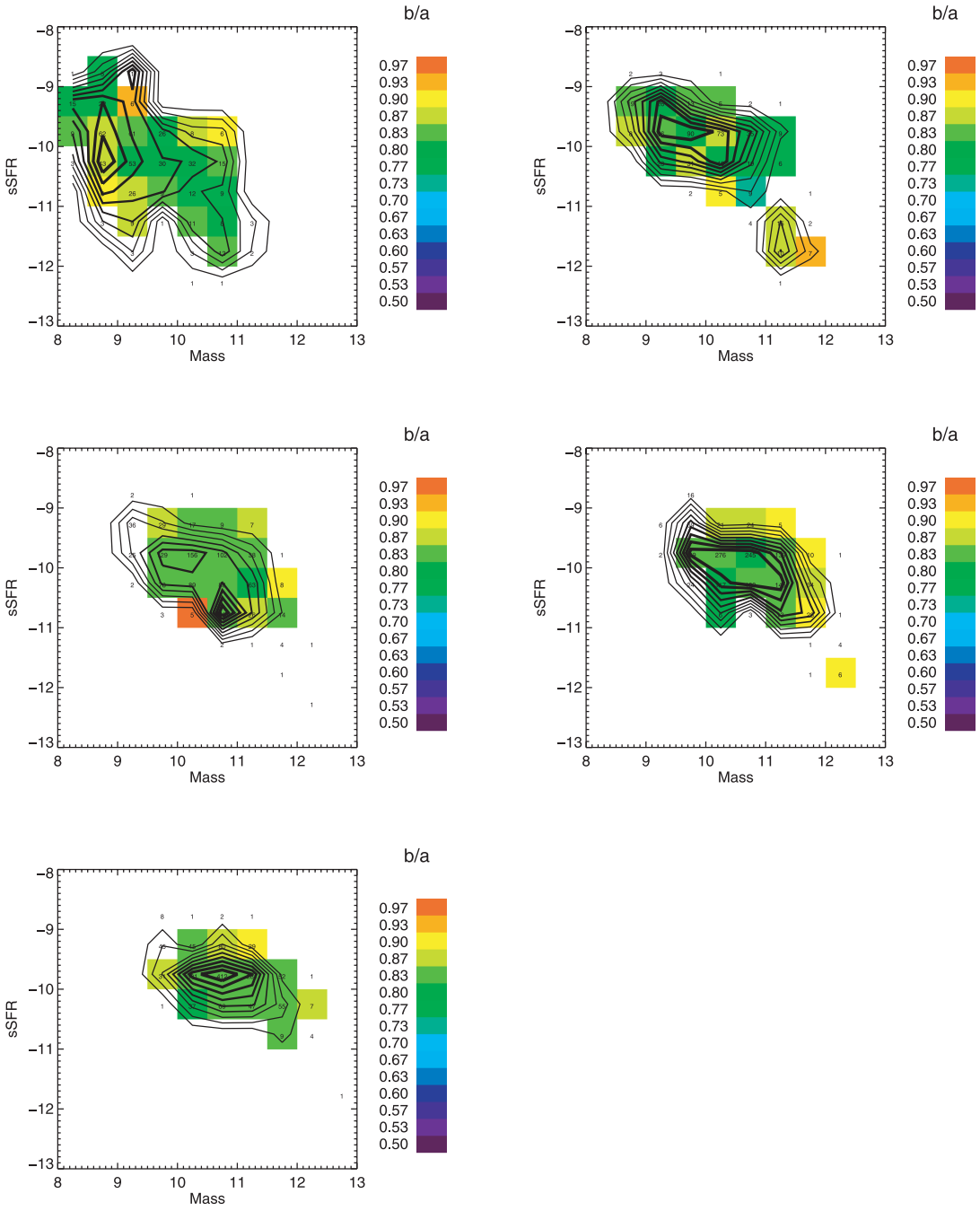

FIG. 11.—Same as Fig. 5, with color coding changed to axis ratio b/a.

The SSFR is given for this model very simply by

$$\mathrm{SSFR} = \frac{1}{\tau}\frac{1}{e^{\xi}-1}, \tag{15}$$

where τ is a function of mass for a coeval population: $\tau = (\mathcal{M}/\mathcal{M}_0)^{-\alpha}(13.47 - t_f)$.

We jointly fit the $\langle \mathrm{IRX} \rangle$ and $\langle \mathrm{SSFR} \rangle$ versus mass and redshift with five free parameters: C_0, t_f, $\mathcal{M}_0$, α, and β. We restrict the fits to the mass range $9.5 \leq \log \mathcal{M} \leq 11.5$, over which the survey appears reasonably complete at all redshifts (see below). There are 46 independent data points and four free parameters. The result is a reasonable fit, with $\chi^2 = 31$, with $C_0 = 4.5$, $t_f = 2.3$ Gyr, $\log \mathcal{M}_0 = 10.58$, $\alpha = 0.72$, and $\beta = 2.1$. Note that for the Schmidt-Kennicutt star formation law we expected $\beta \simeq 1.5$. The fits are displayed in Figures 12 and 13. Using this we predict that the mass-metallicity relation shifts toward higher masses roughly $\Delta(\log \mathcal{M}) \simeq 0.53$ at $z = 0.7$ and 0.75 at $z = 1$, not inconsistent with Savaglio et al. (2005) . This also predicts a peak equivalent extinction at $\xi_{\mathrm{peak}} = \beta = 2.2$ of $A_{\mathrm{FUV,peak}} \simeq 3.0$, or $\langle \mathrm{IRX} \rangle_{\mathrm{peak}} = 1.2$. The only way to distinguish between the closed- and open-box cases is to provide an independent measurement or prediction of the proportionality constant C_0, which is beyond the scope of this paper.

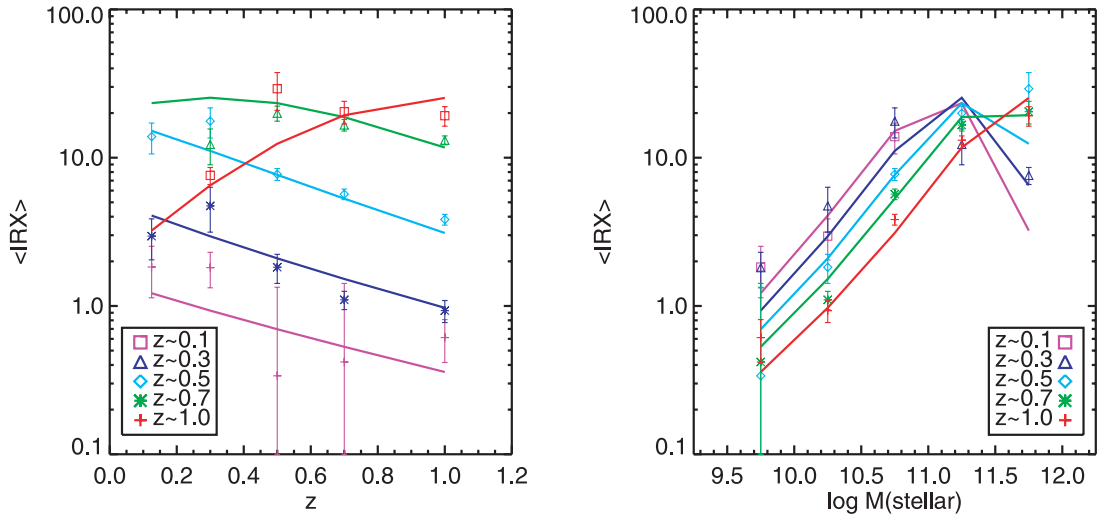

FIG. 12.—Simple SSFR-IRX model fits (*lines*) to $\langle \mathrm{IRX} \rangle$ (linear version plotted on a logarithmic scale) vs. z (*left*) and $\langle \mathrm{IRX} \rangle$ vs. mass (*right*). *Left*: Colors give mass, with $9.5 < \log \mathcal{M} < 10.0$ (*purple*), $10.0 < \log \mathcal{M} < 10.5$ (*blue*), $10.5 < \log \mathcal{M} < 11.0$ (*cyan*), $11.0 < \log \mathcal{M} < 11.5$ (*green*), and $11.5 < \log \mathcal{M} < 12.0$ (*red*). *Right*: Color gives redshift, with $0.05 < z < 0.2$ (*purple*), $0.2 < z < 0.4$ (*blue*), $0.4 < z < 0.6$ (*cyan*), $0.6 < z < 0.8$ (*green*), and $0.8 < z < 1.2$ (*red*).

We show the tight relationship between the age parameter ξ, derived from the stellar mass and the best-fit parameters,

$$\xi(\mathcal{M}, z) = \left(\frac{\mathcal{M}}{10^{10.5}\ \mathcal{M}_{\odot}}\right)^{0.70} \left[\frac{t(z) - 2.37}{t(0) - 2.37}\right], \qquad (16)$$

and the mean IRX in Figure 14. There is an equally tight relationship between the "b-parameter," which in terms of our simple parameterization is

$$b = \langle \mathrm{SSFR} \rangle [t(z) - t(0)] = \frac{\xi}{e^{\xi} - 1}. \qquad (17)$$

This is displayed in Figure 15. Finally, we show the coevolution of $\langle \mathrm{SSFR} \rangle$ and $\langle \mathrm{IRX} \rangle$ in Figure 16.

We can also define a "turnoff" mass where $\xi(\mathcal{M}_t, z) = 1.0$ so that

$$\mathcal{M}_t(z) = 10^{10.5} \left[\frac{t(z) - 2.37}{t(0) - 2.37}\right]^{-1.43}, \qquad (18)$$

which rises from $\log \mathcal{M}_t = 10.5$ at $z = 0$ to $\log \mathcal{M}_t = 11.24$ at $z = 1$. We note that $\log \mathcal{M}_t = 10.5$ is exactly the transition mass between star-forming and passively evolving galaxies noted by Kauffmann et al. (2003) in the SDSS spectroscopic sample.

Metallicity and age are simply related in this picture (see eq. [11]). Johnson et al. (2007) have shown that IRX correlates well with metallicity. The mass-metallicity relationship (Tremonti et al. 2004) is a result of the lower net astration in galaxies with a younger effective age ξ. This simple picture does not predict the observed saturation at high mass. This could be a result of selection effects, since metallicity can only be measured using emission

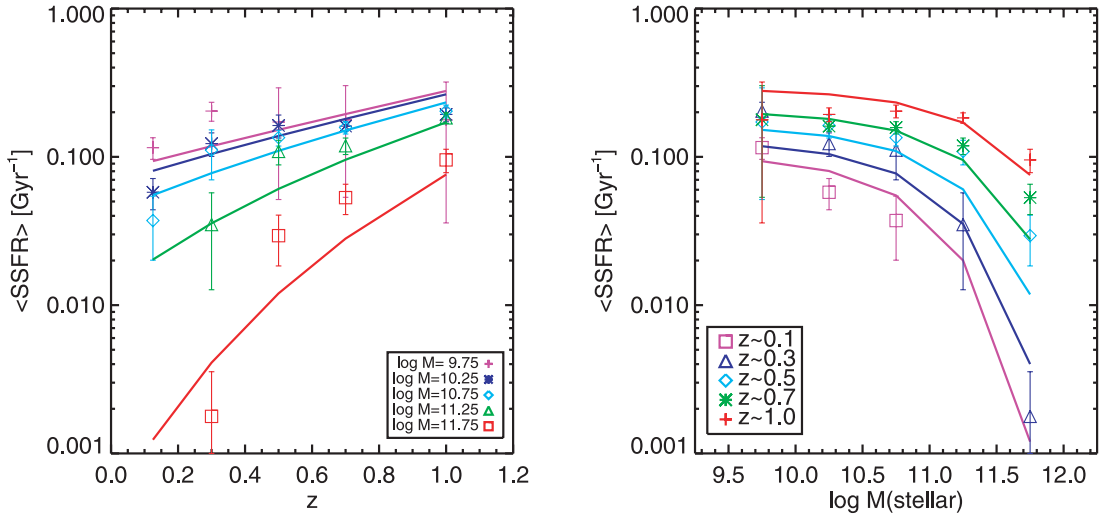

FIG. 13.—Simple SSFR-IRX model fits (*lines*) to $\langle \mathrm{SSFR} \rangle$ vs. z (*left*) and $\langle \mathrm{SSFR} \rangle$ vs. mass (*right*). *Left*: Color gives mass, with $9.5 < \log \mathcal{M} < 10.0$ (*purple*), $10.0 < \log \mathcal{M} < 10.5$ (*blue*), $10.5 < \log \mathcal{M} < 11.0$ (*cyan*), $11.0 < \log \mathcal{M} < 11.5$ (*green*), and $11.5 < \log \mathcal{M} < 12.0$ (*red*). *Right*: Color gives redshift, with $0.05 < z < 0.2$ (*purple*), $0.2 < z < 0.4$ (*blue*), $0.4 < z < 0.6$ (*cyan*), $0.6 < z < 0.8$ (*green*), and $0.8 < z < 1.2$ (*red*).

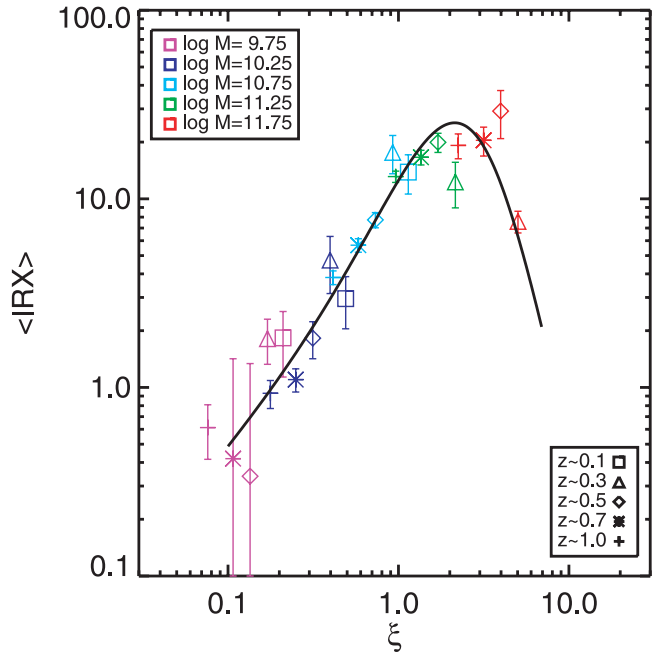

FIG. 14.—IRX (linear version plotted on a logarithmic scale) vs. galaxy age parameter ξ for all masses $9.5 < \log \mathcal{M} < 12.0$ and all redshifts. Color gives mass, with $9.5 < \log \mathcal{M} < 10.0$ (*purple*), $10.0 < \log \mathcal{M} < 10.5$ (*blue*), $10.5 < \log \mathcal{M} < 11.0$ (*cyan*), $11.0 < \log \mathcal{M} < 11.5$ (*green*), and $11.5 < \log \mathcal{M} < 12.0$ (*red*). Symbol type gives redshift, with $0.05 < z < 0.2$ (*plus signs*), $0.2 < z < 0.4$ (*asterisks*), $0.4 < z < 0.6$ (*diamonds*), $0.6 < z < 0.8$ (*triangles*), and $0.8 < z < 1.2$ (*squares*). The solid line is from eqs. (4) and (12).

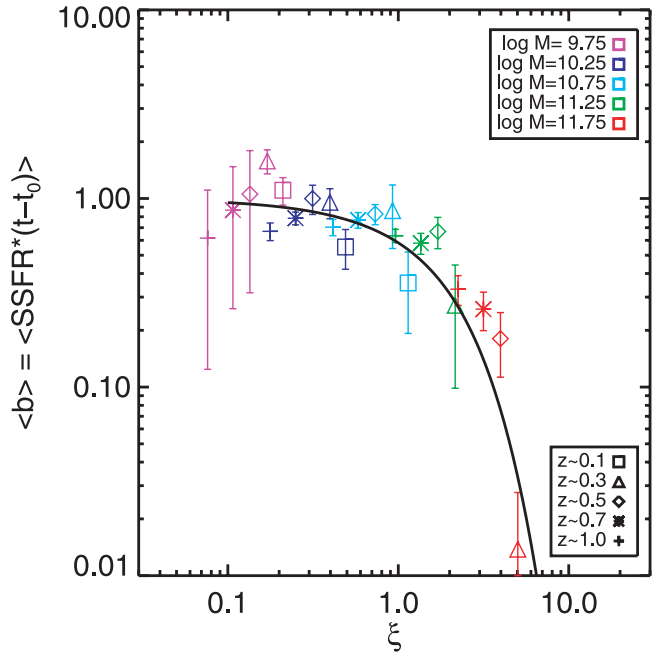

FIG. 15.—Average b-parameter ($\langle$SSFR$\rangle$ multiplied by time since formation t_0) vs. galaxy age parameter ξ for all masses $9.5 < \log \mathcal{M} < 12.0$ and all redshifts. Color gives mass, with $9.5 < \log \mathcal{M} < 10.0$ (*purple*), $10.0 < \log \mathcal{M} < 10.5$ (*blue*), $10.5 < \log \mathcal{M} < 11.0$ (*cyan*), $11.0 < \log \mathcal{M} < 11.5$ (*green*), and $11.5 < \log \mathcal{M} < 12.0$ (*red*). Symbol type gives redshift, with $0.05 < z < 0.2$ (*plus signs*), $0.2 < z < 0.4$ (*asterisks*), $0.4 < z < 0.6$ (*diamonds*), $0.6 < z < 0.8$ (*triangles*), and $0.8 < z < 1.2$ (*squares*). The solid line is from eq. (15).

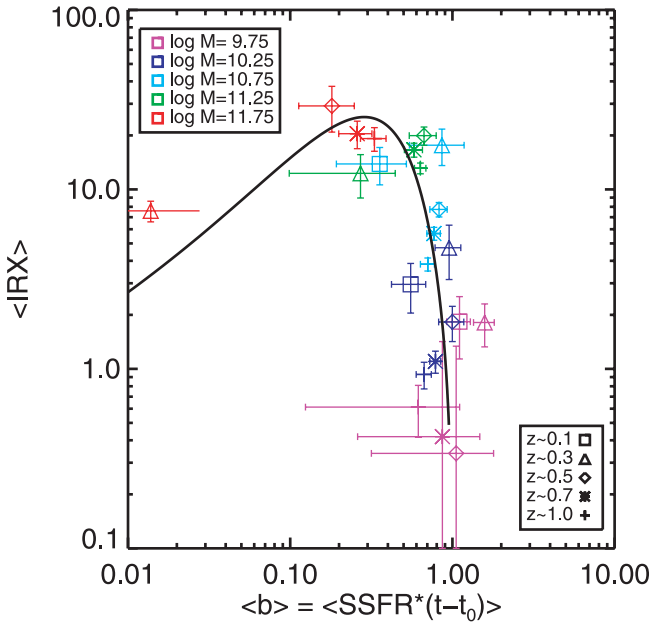

FIG. 16.—IRX (linear version plotted on a logarithmic scale) vs. b-parameter ($\langle$SSFR$\rangle$ multiplied by time since formation t_0) for all masses $9.5 < \log \mathcal{M} < 12.0$ and all redshifts. Color gives mass, with $9.5 < \log \mathcal{M} < 10.0$ (*purple*), $10.0 < \log \mathcal{M} < 10.5$ (*blue*), $10.5 < \log \mathcal{M} < 11.0$ (*cyan*), $11.0 < \log \mathcal{M} < 11.5$ (*green*), and $11.5 < \log \mathcal{M} < 12.0$ (*red*). Symbol type gives redshift, with $0.05 < z < 0.2$ (*plus signs*), $0.2 < z < 0.4$ (*asterisks*), $0.4 < z < 0.6$ (*diamonds*), $0.6 < z < 0.8$ (*triangles*), and $0.8 < z < 1.2$ (*squares*). The solid line is from eqs. (4), (12), and (15).

lines in galaxies with a high SSFR. It is plausible that transition galaxies with low emission line equivalent widths display a higher metallicity than the actively star-forming sample at high mass. It could also indicate a second quenching mechanism in addition to simple gas exhaustion, or a more complex enrichment picture than simple closed-box evolution.

5.2. *Star Formation History and Evolution of the Blue and Red Sequence*

We begin by determining the mass function by summing over the SSFR in the bivariate mass-SSFR function. The distribution in each redshift bin is displayed in Figure 17. The error bars include Poisson and cosmic variance, the latter from Somerville et al. (2004). Note that these combined errors will be highly correlated between mass bins at a given redshift. This correlation is not well represented by the plotted error bars, since there is large covariance between mass bins in a given redshift bin. Note also that there is evidence for incompleteness in the lowest mass bin ($\log \mathcal{M} = 9.75$) for $z = 1.0$. Mass bins $\log \mathcal{M} \leq 9.25$ were not used in the modeling of the previous section, because of obvious incompleteness.

We model the mass function as an evolving Schechter function:

$$\phi(\mathcal{M}, z) = (\ln 10)\phi_*(z)\left[\frac{\mathcal{M}}{\mathcal{M}(z)}\right]^{\alpha} \exp\left[-\frac{\mathcal{M}}{\mathcal{M}(z)}\right], \quad (19)$$

where $\mathcal{M}_*(z) = \mathcal{M}_*(0)(1+z)^{\beta}$ and $\phi_*(z) = \phi_*(0)(1+z)^{\gamma}$. We use a version of χ^2 minimization that accounts for the cosmic variance and covariance between mass bins in a single redshift bin (e.g., Newman & Davis 2002) The best-fit parameters and

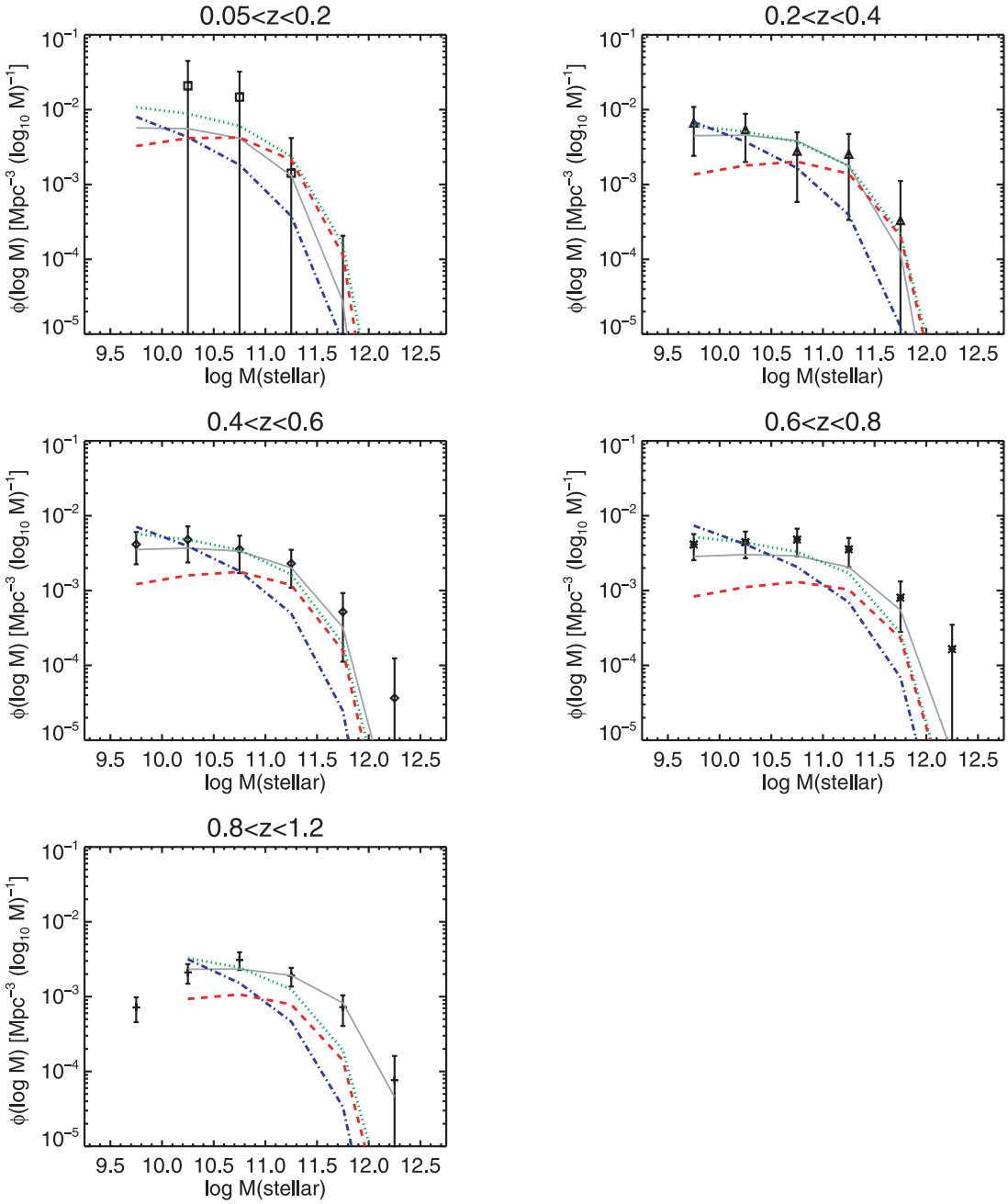

FIG. 17.—Mass distribution function $\phi(\log \mathcal{M})$ vs. $\log \mathcal{M}$ in each redshift bin. Points and error bars give the mass function derived in this paper. The solid line gives the result of the fit to the evolving Schechter function. Colored lines give the Schechter functions derived by Borch et al. (2006). The green dotted line is for the entire galaxy sample, red for the red-sequence galaxies, and blue for the blue-cloud galaxies. Note that the $z = 0$ point is from Bell et al. (2003), and our $z \sim 1.0$ bin is compared to the Borch et al. (2006) $z = 0.9$ bin.

1 σ errors (obtained by marginalizing over other parameters) are

$$\phi_*(0) = \left(0.0040^{+0.0036}_{-0.0023}\ \mathrm{Mpc}^{-3}\right) \log \mathcal{M}^{-1}, \quad (20)$$

$$\log \mathcal{M}_*(0) = 10.86^{+0.33}_{-0.43}, \quad (21)$$

$$\alpha = -0.93^{+0.11}_{-0.10}, \quad (22)$$

$$\beta = 2.4^{+1.2}_{-1.0}, \quad (23)$$

$$\gamma = -1.5^{+0.5}_{-1.1}. \quad (24)$$

The nonzero values of β and γ indicate evolution in the characteristic mass and the number density, although cosmic variance prevents tight constraints on the evolutionary indices. Note we have not parameterized an evolving low-mass slope.

We can compare the results of this mass function analysis with the results of Bell et al. (2003) using a much larger cosmic volume at $z \sim 0.15$. Converted to our cosmology and corrected upward to a nondiet Salpeter IMF (simply dividing their result by 0.7), they obtain $\phi_* = (0.0035\ \mathrm{Mpc}^{-3}) \log \mathcal{M}^{-1}$ for all galaxies and $\phi_* = (0.0020\ \mathrm{Mpc}^{-3}) \log \mathcal{M}^{-1}$ for late-type galaxies, and $\log \mathcal{M}_* = 11.17$ and 11.06 for all galaxies and late-type galaxies, respectively, versus our values at $z = 0.125$: $\phi_* = \left(0.0040^{+0.0036}_{-0.0023}\ \mathrm{Mpc}^{-3}\right) \log \mathcal{M}^{-1}$ and $\log \mathcal{M}_* = 10.86$. The mass cutoff is in fair agreement, but our density is a factor of 2 larger if we compare to just their late-type (morphologically selected)

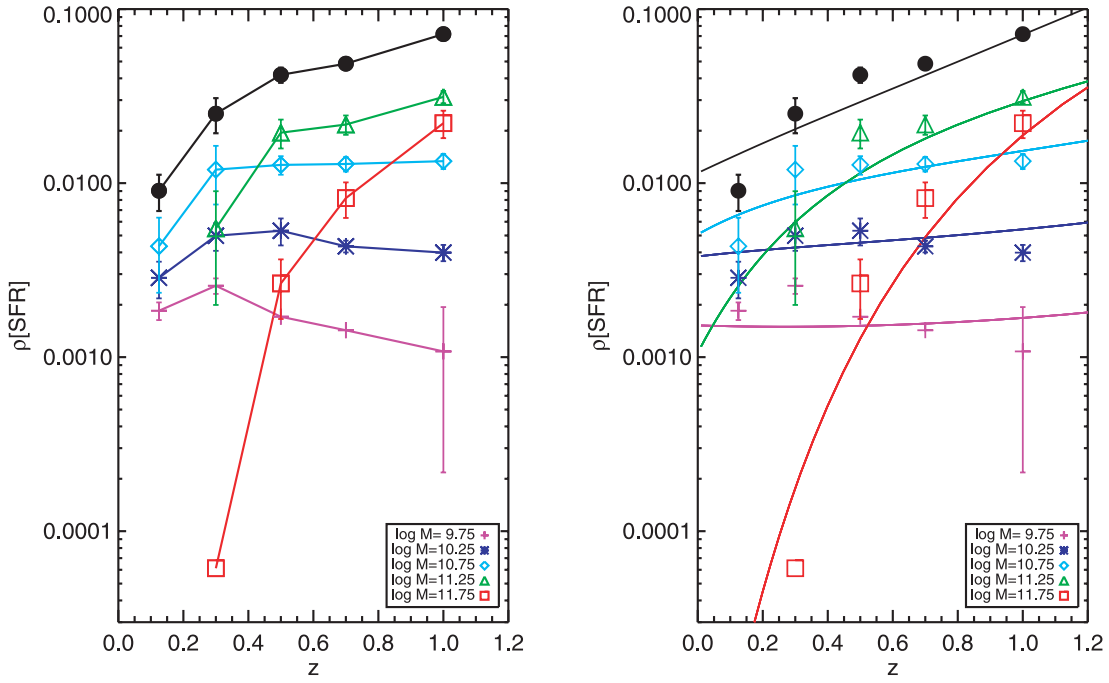

FIG. 18.—Star formation rate density [$\mathcal{M}_\odot$ yr^{-1} Mpc^{-3}] vs. redshift derived assuming a nonevolving mass function. Error bars are based on bootstrapping but do not include cosmic variance, which adds a relative error of 0.37 to all the measurements. *Left*: Density in each mass bin, with $9.5 < \log \mathcal{M} < 10.0$ (*purple*), $10.0 < \log \mathcal{M} < 10.5$ (*blue*), $10.5 < \log \mathcal{M} < 11.0$ (*cyan*), $11.0 < \log \mathcal{M} < 11.5$ (*green*), $11.5 < \log \mathcal{M} < 12.0$ (*red*), and total (*black*). *Right*: Compared with a simple IRX-SSFR model, for each mass bin (colors are as in the left panel) and for the total (*black*).

sample. The mass cutoff, slope, and density parameters are highly correlated, and indeed if we fix our mass cutoff ($z = 0$) at 11.1 (which is within our errors) we find $\phi_* = (0.0025\ \mathrm{Mpc}^{-3}) \times \log \mathcal{M}^{-1}$, close to the Bell et al. (2003) value. If we fix the slope to $\alpha = -1.1$ we find $\phi_* = (0.0020\ \mathrm{Mpc}^{-3}) \log \mathcal{M}^{-1}$ and $\log \mathcal{M}_* = 11.1$. Thus, our results at $z \sim 0$ are consistent with those of Bell et al. (2003) within the errors quoted above (dominated by cosmic variance).

We can also compare to the evolving Borch et al. (2006) mass function, which uses all three COMBO-17 fields with a total of 25,000 galaxies. We correct their masses to our standard Salpeter IMF by multiplying by 1.8, as they suggest. At $z = 0.9$ they obtain $\phi_*(z = 0.9) = (0.0012\ \mathrm{Mpc}^{-3}) \log \mathcal{M}^{-1}$ for all galaxies and $\phi_*(z = 0.9) = (0.0005\ \mathrm{Mpc}^{-3}) \log \mathcal{M}^{-1}$ for blue, color-selected galaxies, and $\log \mathcal{M}_* = 11.08$ and 11.00 for all galaxies and blue, color-selected galaxies, respectively. Using our evolutionary parameters we find $\phi_*(z = 0.9) = (0.0015\ \mathrm{Mpc}^{-3}) \log \mathcal{M}^{-1}$ and $\log \mathcal{M}_*(z = 0.9) = 11.54$. Our results are compared to those of Borch et al. (2006) in Figure 17. Surprisingly, our results agree well with theirs for the entire galaxy sample in all but the highest redshift bin. Our bin extends over $0.8 < z < 1.2$, while theirs is $0.8 < z < 1.0$. Our mass function shows a distinctly higher mass cutoff in the two highest redshift bins, which leads to the stronger evolution in the characteristic mass.

Searching for an explanation of this difference, we note that a significant fraction of our sample has red colors. In the lowest redshift bin this is true even after the extinction correction. For example, if we eliminate galaxies with $\langle \mathrm{SSFR} \rangle < 10^{-10.5}$, corresponding to corrected $(\mathrm{NUV} - H)_{0,\mathrm{AB}} > 4.25$, which from Figure 3 can be seen to exclude the tail of the distribution, the mass function density parameter at $z = 0$ falls by a factor of 2. This suggests that a significant fraction of the mass (and even the star formation rate) at low redshift is locked in high-mass galaxies with low SSFRs and red intrinsic (unextincted) colors. Some of these galaxies could be classified as early-type in Bell et al. (2003) because their observed colors are even redder (as they are massive and exhibit high IRX), while their morphologies could be dominated by an evolved, bulgelike component. The steepness of the slope parameter obtained for color-selected blue samples (Bell et al. 2003) could also be a reflection of excluding extincted, reddened, higher mass galaxies and transition galaxies that still show some star formation.

The characteristic mass increases with redshift, with $\Delta \log \mathcal{M} = 0.7 \pm 0.4$, which can be compared to the model change of $\log \mathcal{M}_t$ from 10.5 to 11.24. Thus, the blue-sequence mass function shows directly the effects of downsizing. The total mass of the blue sequence obtained by integrating the mass function is a declining function of redshift (since $\beta > -\gamma$): $\rho_{\mathcal{M}} \simeq 4.8 \times 10^8 \rightarrow 2.8 \times 10^8\ \mathcal{M}_\odot\ \mathrm{Mpc}^{-3}$ (from $z = 0.8$ to 0). Others (Borch et al. 2006; Blanton 2006) have found that the blue-sequence mass is constant with time, and given the uncertainty our results are not inconsistent with this conclusion. In our model this occurs because the mass of the blue sequence is moving from fewer massive galaxies to larger numbers of lower mass galaxies. The decrease in blue luminosity density (e.g., Bell et al. 2004; Faber et al. 2007) is a result of an increase in mass-to-light ratio due in turn to the falloff of the SSFR. The total stellar mass appears to remain constant or decline in spite of the formation of new stars. Before exploring this point, we estimate the star formation rate density and its evolution.

In order to calculate the star formation rate history while minimizing the effects of cosmic variance, we renormalize the observed mass function to the fit given in Figure 17 and equation (20) for all redshift bins. The results in each mass bin and the total are shown in Figure 18. We also calculate the star formation rate density evolution for the simple exponential model of the previous section. This is shown in Figure 18 (*right*). Apparently, the dominant galaxy population responsible for the fall in SFR density from $z = 1$ to 0 is $10.5 < \log \mathcal{M} < 11.5$ (*cyan and green*

symbols). This is consistent with the conclusion that the characteristic mass $\mathcal{M}_c$ derived in the previous section evolves from $10^{10.5}$ to $10^{11.25}$. Zheng et al. (2007), also using COMBO-17 and *Spitzer* data and the stacking technique of Zheng et al. (2006), have reached conclusions that in many ways are similar to ours, but differ in some important details. In particular, they find that the SFR in the highest mass bin ($\log \mathcal{M} < 11.25$ when converted to our IMF) does not fall more steeply than those in the lower mass bins.

Stars formed over $0 < z < 1$ will increase the total mass of the blue sequence unless these galaxies transition to the red sequence. In order to maintain the constant or declining blue-sequence mass, we calculate that the average mass flux over $0 < z < 1$ must be $\rho_{B\rightarrow R} \simeq 0.03$–$0.05\ \mathcal{M}_\odot\ \mathrm{yr}^{-1}\ \mathrm{Mpc}^{-3}$. This is in agreement with the value we obtained by examining transition galaxies at $z \sim 0.1$ (Martin et al. 2007).

6. SUMMARY

We have used COMBO-17, *Spitzer*, and *GALEX* data to study the coevolution of the IRX and star formation for galaxies over the mass range of $9.5 < \log \mathcal{M} < 12.0$ and the redshift range $0 < z < 1.2$. We have reached a number of interesting conclusions:

1. The IRX grows with stellar mass in a way that mirrors the mass-metallicity relationship. The rise of the IRX with mass saturates at a characteristic mass, above which it appears to fall.
2. The SSFR is roughly constant up to the same characteristic mass, above which it falls steeply.
3. The characteristic mass grows with redshift.
4. At a given mass below the characteristic mass, the IRX grows with redshift.
5. The mass and evolutionary trends of the IRX and SSFR are reasonably fit by a simple gas-exhaustion model in which the IRX is determined by gas surface density and metallicity, the metallicity grows with time following a closed-box model, and the SFR is determined by the exponentially falling gas density. The SFR time constant scales with the mass as $\tau \sim \mathcal{M}^{-0.7}$.
6. The characteristic mass is a "turnoff" mass indicating galaxies that are starting to move off the blue sequence.
7. The mass-metallicity relationship is understood to be determined largely by the characteristic age of the galaxies. The mass-IRX relationship is also influenced by gas exhaustion above the turnoff mass.
8. The factor of 6–8 rise in SFR density to $z = 1$ is predominantly due to galaxies in the mass range $10.5 < \log \mathcal{M} < 11.5$, the turnoff mass over the $0 < z < 1$ redshift range.

These observations show directly the steady buildup of heavy elements in the interstellar media of evolving galaxies, and that the infrared excess represents an excellent tool for selecting similar-mass galaxies at various stages of evolution. In particular, galaxies at early stages in their evolution can be selected by their low IRX (Fig. 14).

It is important to stress that these trends were uncovered by considering the average properties, notably the IRX, of large numbers of galaxies. A more sophisticated treatment would study the detailed distribution of properties, for example, the spread in SSFR in a given mass bin. A simple scaling model of course predicts no spread at all for a coeval population. This distribution may yield information about the burst and formation history of galaxies. For example, it will be very interesting to study galaxies with unusually low IRX values at a given epoch and mass to determine whether they have been more recently formed. It will also be interesting to compare this very simple picture with the results of semianalytic models combined with the latest numerical simulations. Finally, it is critical to improve the observational basis of this work, most notably with a better understanding of the FIR bolometric correction and its evolution, with a larger and deeper sample of galaxies, and by extending the redshift range of this approach to determine whether this simple picture continues to apply during the major epoch of star formation.

GALEX (*Galaxy Evolution Explorer*) is a NASA Small Explorer, launched in 2003 April. We gratefully acknowledge NASA's support for construction, operation, and science analysis for the *GALEX* mission, developed in cooperation with the Centre National d'Etudes Spatiales of France and the Korean Ministry of Science and Technology.

Facilities: GALEX, Sloan

REFERENCES

Adelberger, K. L., & Steidel, C. C. 2000, ApJ, 544, 218
Bell, E. F., McIntosh, D. H., Katz, N., & Weinberg, M. D. 2003, ApJS, 149, 289
Bell, E. F., et al. 2004, ApJ, 608, 752
———. 2005, ApJ, 625, 23
Bertin, E., & Arnouts, S. 1996, A&AS, 117, 393
Binney, J., & Merrifield, M. 1998, Galactic Astronomy (Princeton: Princeton Univ. Press)
Blanton, M. 2006, ApJ, 648, 268
Borch, A., et al. 2006, A&A, 453, 869
Brinchmann, J., & Ellis, R. S. 2000, ApJ, 536, L77
Bruzual, G., & Charlot, S. 2003, MNRAS, 344, 1000
Calzetti, D., Armus, L., Bohlin, R. C., Kinney, A. L., Koornneef, J., & Storchi-Bergmann, T. 2000, ApJ, 533, 682
Cowie, L. L., Songaila, A., Hu, E. M., & Cohen, J. G. 1996, AJ, 112, 839
Dale, D. A., & Helou, G. 2002, ApJ, 576, 159
Efron, B. 1979, Ann. Stat., 7, 1
Faber, S. M., et al. 2007, ApJ, 665, 265
Gardner, J. P., Brown, T. M., & Ferguson, H. C. 2000, ApJ, 542, L79
Gordon, K. D., et al. 2005, PASP, 117, 503
Hartwick, F. D. A. 1976, ApJ, 209, 418
Johnson, B., et al. 2006, ApJ, 644, L109
———. 2007, ApJS, 173, 377
Kauffmann, G., et al. 2003, MNRAS, 341, 54
Kennicutt, R. C., Jr. 1989, ApJ, 344, 685
———. 1998, ARA&A, 36, 189
Martin, D. C., et al. 2005, ApJ, 619, L1
Martin, D. C., et al. 2007, ApJS, 173, 342
Meurer, G. R., Heckman, T. M., & Calzetti, D. 1999, ApJ, 521, 64
Morrissey, P., et al. 2005, ApJ, 619, L7
———. 2007, ApJS, 173, 682
Newman, J. A., & Davis, M. 2002, ApJ, 564, 567
Noeske, K. G., et al. 2007, ApJ, 660, L47
Papovich, C., et al. 2006, ApJ, 640, 92
Pérez-González, P. G., et al. 2005, ApJ, 630, 82
Reddy, N. A., Steidel, C. C., Fadda, D., Yan, L., Pettini, M., Shapley, A. E., Erb, D. K., & Adelberger, K. L. 2006, ApJ, 644, 792
Savaglio, S., et al. 2005, ApJ, 635, 260
Schiminovich, D., et al. 2005, ApJ, 619, L47
Searle, L., & Sargent, W. L. W. 1972, ApJ, 173, 25
Somerville, R. S., Lee, K., Ferguson, H. C., Gardner, J. P., Moustakas, L. A., & Giavalisco, M. 2004, ApJ, 600, L171
Tinsley, B. M. 1968, ApJ, 151, 547
Tremonti, C. A., et al. 2004, ApJ, 613, 898
Wang, B., & Heckman, T. M. 1996, ApJ, 457, 645
Wolf, C., Meisenheimer, K., Rix, H.-W., Borch, A., Dye, S., & Kleinheinrich, M. 2003, A&A, 401, 73
Wolf, C., et al. 2004, A&A, 421, 913
Wyder, T., et al. 2007, ApJS, 173, 293
Zheng, X. Z., Bell, E. F., Papovich, C., Wolf, C., Meisenheimer, K., Rix, H.-W., Rieke, G. H., & Somerville, R. 2007, ApJ, 661, L41
Zheng, X. Z., Bell, E. F., Rix, H.-W., Papovich, C., Le Floc'h, E., Rieke, G. H., & Pérez-González, P. G. 2006, ApJ, 640, 784